

<sup>1</sup> **MicroBooNE: Neutron Induced Cosmogenic  $\pi^0$ s**

<sup>2</sup> **Ryan A.Grosso**

<sup>3</sup> Submitted in partial fulfillment of the

<sup>4</sup> requirements for the degree

<sup>5</sup> of Doctor of Philosophy

<sup>6</sup> in the Graduate School of Arts and Sciences

<sup>7</sup> **UNIVERSITY OF CINCINNATI**

<sup>8</sup> 2018

9

10

©2018

11

Ryan A.Grosso

12

All Rights Reserved

# <sup>13</sup> Table of Contents

<sup>14</sup>	<b>List of Figures</b>	iii
<sup>15</sup>	<b>List of Tables</b>	v
<sup>16</sup>	<b>1 Introduction</b>	1
<sup>17</sup>	<b>2 Neutrinos &amp; Neutrino Oscillations</b>	3
<sup>18</sup>	2.1 The History the Neutrino . . . . .	3
<sup>19</sup>	2.2 Discovery of the Neutrino . . . . .	5
<sup>20</sup>	2.3 Neutrinos in the Standard Model . . . . .	8
<sup>21</sup>	2.4 Neutrino Interactions . . . . .	9
<sup>22</sup>	2.5 Neutrino Mass and Flavor Oscillations . . . . .	12
<sup>23</sup>	2.6 Sterile Neutrinos . . . . .	17
<sup>24</sup>	<b>3 The MicroBooNE Detector</b>	18
<sup>25</sup>	3.1 Brief History of LAR-TPC's . . . . .	18
<sup>26</sup>	3.2 Introduction . . . . .	19
<sup>27</sup>	3.3 Time Projection Chamber . . . . .	20
<sup>28</sup>	3.4 Light Collection . . . . .	26
<sup>29</sup>	3.5 Electronics Readout . . . . .	28
<sup>30</sup>	<b>4 Booster Neutrino Beam</b>	30
<sup>31</sup>	4.1 Primary Beam, Target and Horn . . . . .	31
<sup>32</sup>	4.2 Neutrino Flux Prediction . . . . .	33

<sup>33</sup>	<b>5 Low Energy Excess and Relevant Cross Sections</b>	<b>35</b>
<sup>34</sup>	5.1 Overview . . . . .	35
<sup>35</sup>	5.2 LSND Excess . . . . .	35
<sup>36</sup>	5.3 MiniBooNE Excess . . . . .	37
<sup>37</sup>	5.4 Neutral Current $\pi^0$ production . . . . .	38
<sup>38</sup>	5.5 NC- $\pi^0$ in Carbon vs Argon . . . . .	40
<sup>39</sup>	<b>6 Cosmogenic <math>\pi^0</math>s at MicroBooNE</b>	<b>41</b>
<sup>40</sup>	6.1 Motivation . . . . .	41
<sup>41</sup>	6.2 Traditional Reconstruction . . . . .	43
<sup>42</sup>	6.3 Wire Cell Imaging . . . . .	44
<sup>43</sup>	6.4 Pattern Recognition . . . . .	45
<sup>44</sup>	6.5 Clustering . . . . .	46
<sup>45</sup>	6.6 Track and Shower Selection . . . . .	48
<sup>46</sup>	6.6.1 Track Removal . . . . .	48
<sup>47</sup>	6.6.2 Single $\pi^0$ Reconstruction . . . . .	48
<sup>48</sup>	6.7 Single $\pi^0$ cosmic sample . . . . .	52
<sup>49</sup>	<b>7 Results</b>	<b>56</b>
<sup>50</sup>	7.1 Monte Carlo Simulation . . . . .	56
<sup>51</sup>	7.2 Data . . . . .	59
<sup>52</sup>	7.3 Data-Monte Carlo Comparison . . . . .	59
<sup>53</sup>	<b>8 Conclusions</b>	<b>62</b>
<sup>54</sup>	8.1 Conclusion . . . . .	62
<sup>55</sup>	<b>I Appendices</b>	<b>63</b>
<sup>56</sup>	<b>Bibliography</b>	<b>66</b>

# <sup>57</sup> List of Figures

58	2.1 Cowan and Reines first proposed neutrino experiment. . . . .	5
59	2.2 The hadron production cross section around the $Z^0$ resonance from LEP. . . . .	7
60	2.3 The Standard Model . . . . .	9
61	2.4 Charge and Neutral Current Interactions . . . . .	12
62	2.5 This plot shows the appearance and disappearance curves for a 2-flavor ap-	
63	proximation as a function of baseline. The values of $\Delta m^2 = 0.0025 \text{ eV}^2$	
64	and $\sin^2 \theta = 0.14$ are used. . . . .	14
65	2.6 Neutrino Mass Hierarchy . . . . .	16
66	3.1 Diagram of a Time Projection Chamber . . . . .	19
67	3.2 MicroBooNE TPC . . . . .	21
68	3.3 MicroBooNE wires measured linear mass density . . . . .	22
69	3.4 Tensioning system . . . . .	23
70	3.5 Multiple wire planes installed in MicroBooNE . . . . .	24
71	3.6 MicroBooNE tension measuring device . . . . .	25
72	3.7 MicroBooNE tension map . . . . .	26
73	3.8 MicroBooNE tension histogram . . . . .	26
74	3.9 PMT optical unit . . . . .	27
75	3.10 PMT optical unit . . . . .	28
76	3.11 Detector Electronic layout . . . . .	29
77	4.1 The Booster Neutrino Campus . . . . .	30
78	4.2 BNB Target . . . . .	32

79	4.3	Booster Neutrino Beamline . . . . .	33
80	4.4	BNB Target . . . . .	34
81	5.1	LSND Excess . . . . .	36
82	5.2	MiniBooNE Event topology . . . . .	38
83	5.3	MiniBooNE excess for $\nu$ and $\bar{\nu}$ . . . . .	39
84	5.4	Neutrino induces single $\pi^0$ production . . . . .	40
85	6.1	Icarus Cosmic $\pi^0$ . . . . .	43
86	6.2	Wire Cell reconstruction of CORSIKA MC viewed in the BEE viewer . . . . .	46
87	6.3	Photon distribution from $\pi^0$ s . . . . .	49
88	6.4	Reconstructed energy sum and energy product for shower pairs. Both, the reconstructed energy sum and product is less than the true energy deposited.	50
90	6.5	Reconstructed vs. True opening angle . . . . .	51
91	6.6	Single particle $\pi^0$ mass distribution . . . . .	52
92	6.7	Single particle $\pi^0$ reconstruction efficiency . . . . .	53
93	6.8	Cosmic $\pi^0$ production by parent process . . . . .	54
94	6.9	Spatial decay points for cosmic $\pi^0$ s in MicroBooNE . . . . .	55
95	7.1	Enhanced Signal Sample . . . . .	58
96	7.2	Background Sample . . . . .	59
97	7.3	Area normalized Data-Monte Carlo mass distributions . . . . .	60
98	7.4	Direct data Monte Carlo rate comparison . . . . .	61
99	7.5	Direct data Monte Carlo rate comparison . . . . .	61

# <sup>100</sup> List of Tables

<sup>101</sup>	4.1 Beam Production Systematics . . . . .	34
<sup>102</sup>	7.1 CORSIKA MC rates . . . . .	57

# <sup>103</sup> Chapter 1

## <sup>104</sup> Introduction

<sup>105</sup> This thesis describes work towards electromagnetic shower reconstruction and steps towards  
<sup>106</sup> a neutral current single  $\pi^0$  cross section measurement motivated from reconstruction tech-  
<sup>107</sup> niques used for neutron induced cosmogenic  $\pi^0$  analysis. This thesis will use data from  
<sup>108</sup> the MicroBooNE Liquid Argon Time Projection Chamber (LArTPC) located at the Fermi  
<sup>109</sup> National Accelerator in Batavia, IL.

<sup>110</sup>

<sup>111</sup> To begin, Chapter 2 will provide some background about the neutrino. We will begin by  
<sup>112</sup> presenting the initial premise for the need of a neutrino-like particle. Then, we will describe  
<sup>113</sup> the theoretical framework used to address how they interact the standard model. Finally we  
<sup>114</sup> will present the phenomenon known as neutrino oscillation and provide some mathematical  
<sup>115</sup> framework to describe it. Chapter 3 begins with a brief history of the LArTPC detector  
<sup>116</sup> technology and its use as a high precision neutrino detector. The chapter continues to  
<sup>117</sup> explain in depth the various subsystems that constitute the MicroBooNE detector. Chapter  
<sup>118</sup> 4 will describe how a neutrino beam is produced and delivered to the MicroBooNE detector.  
<sup>119</sup> It will focus on Fermilab's Booster Neutrino Beam (BNB) which generates a beam of nearly  
<sup>120</sup> pure  $\nu_\mu$  or  $\bar{\nu}_\mu$  around 1 GeV in average energy. Chapter 5 will present in detail the claims  
<sup>121</sup> of the electromagnetic  $\nu_e$ -like excess first seen by the LSND experiment and then later  
<sup>122</sup> verified by the MiniBooNE experiment. This chapter will also discuss the neutral current  
<sup>123</sup> cross section, which is the main background in the MiniBooNE excess claim. Chapter  
<sup>124</sup> 6 will introduce MicroBooNE's cosmogenic background and motivate the importance of

understanding the cosmic rate. Here, we will also discuss the motivation to use cosmic  $\pi^0$  events as a means of calibrating the detector energy scale. The cosmic backgrounds are addressed for the oscillation analysis and a future neutral current single  $\pi^0$  measurement. Next, this chapter will address simulation, reconstruction, and event selection. Chapter 7 will present results from MicroBooNE cosmics data addressing the cosmic  $\pi^0$  rate from neutral induced events. Finally, we will conclude with some

## <sup>131</sup> Chapter 2

# <sup>132</sup> Neutrinos & Neutrino Oscillations

### <sup>133</sup> 2.1 The History the Neutrino

<sup>134</sup> The story of the neutrino began in Paris on a cloudy winter day in the year 1896. Parisian  
<sup>135</sup> native, Henri Becquerel was experimenting with uranium salts and investigating the newly  
<sup>136</sup> discovered x-ray radiation. [1] He hypothesized that when the salts were energized by sun-  
<sup>137</sup> light they would produce the x-ray radiation. This hypothesis was disproven on the cloudy  
<sup>138</sup> February 27th day when his experiment still detected radiation emitting from the salts in  
<sup>139</sup> the absence of the sun. Becquerel had discovered radioactivity. In the coming years, this  
<sup>140</sup> phenomena was supported by the work of Marie and Pierre Curie in studying the radioac-  
<sup>141</sup> tivity of the element Thorium which lead to their discovery of the elements Polonium and  
<sup>142</sup> Radium. These discoveries would later win Becquerel and the Curie's the 1903 Nobel Prize  
<sup>143</sup> in Physics.

<sup>144</sup>

<sup>145</sup> After radioactivity became an accepted phenomena in the science community, Ernst  
<sup>146</sup> Rutherford discovered that radioactive decay products came in two different forms. He  
<sup>147</sup> labeled them as  $\alpha$ -decay and  $\beta$ -decay. At the time, beta decay was believed to be a two body  
<sup>148</sup> decay where a nucleus  $A$  decays into a lighter nucleus  $A'$  and a  $\beta$ -particle(electron). The  
<sup>149</sup> outgoing energy of the electron from a two body decay is given by equation 2.1. Assuming  
<sup>150</sup> conservation of energy, the value of the outgoing energy should be a discrete.

$$E_e = \frac{m_A^2 + me^2 - m_{A'}^2}{2m_A} \quad (2.1)$$

151 In 1914, James Chadwick had discovered that the energy spectrum of the  $\beta$ -particles  
 152 were continuations as opposed to mono-energetic. While some scientist were willing to  
 153 abandon the requirement of energy conservation, others found this to be an unpalatable  
 154 solution. Unable to attend the 1930 Tubingen physics conference in Germany, Wolfgang  
 155 Pauli wrote a letter to the attendees in which he proposed the first idea of the neutrino.  
 156 An excerpt from his famous December 4th letter is translated from German below [2].

157 I have hit upon a desperate remedy to save the “exchange theorem” of statistics  
 158 and the law of conservation of energy. Namely, the possibility that there could  
 159 exist in the nuclei electrically neutral particles, that I wish to call neutrons,  
 160 which have spin 1/2 and obey the exclusion principle and which further differ  
 161 from light quanta in that they do not travel with the velocity of light. The  
 162 mass of the neutrons should be of the same order of magnitude as the electron  
 163 mass and in any event not larger than 0.01 proton masses. The continuous beta  
 164 spectrum would then become understandable by the assumption that in beta  
 165 decay a neutron is emitted in addition to the electron such that the sum of the  
 166 energies of the neutron and the electron is constant...

167 In 1932, Chadwick discovered the neutron we know of today. Unfortunately, this neutron  
 168 was too heavy to be the particle that Pauli had proposed. Expanding on Pauli’s work, Enrico  
 169 Fermi proposed a more complete picture of beta decay and renamed Pauli’s ‘neutron’ to  
 170 what is commonly called a *neutrino*. Fermi’s theory directly coupled the neutron with a  
 171 final state proton, electron, and neutrino. This theory of beta decay,  $n \rightarrow p + e^- + \bar{\nu}_e$   
 172 preserves the law of conservation of energy and would later prove to be a more accurate  
 173 descriptor of the process.

## <sup>174</sup> 2.2 Discovery of the Neutrino

<sup>175</sup> Measuring and detecting neutrinos is a tricky business. In the 1950's, Clyde Cowan and  
<sup>176</sup> Frederick Reines set out to directly measure neutrino interactions for the first time. If a free  
<sup>177</sup> neutrino existed, they hypothesized that they could detect the byproducts from the inverse  
<sup>178</sup> beta decay  $\bar{\nu}_e + p \rightarrow e^+ + n$ . They realized that such a measurement would require a very  
<sup>179</sup> intense neutrino source and a large detector. Their first proposal, which was approved, was  
<sup>180</sup> to detonate a nuclear bomb to supply the large, instantaneous source of neutrinos. A large  
<sup>181</sup> detector filled with liquid scintillator would free fall down a mine shaft recording flashes  
<sup>182</sup> of light from the ionizing positrons before landing on a bed of feathers and foam rubber.  
<sup>183</sup> The original experimental schematic is shown in Figure 2.1. At that time, the theorized  
<sup>184</sup> neutrino cross section was  $10^{-43} \text{ cm}^2/\text{proton}$  while the existing measured limit was still 7  
<sup>185</sup> orders of magnitude short in sensitivity. The bomb experiment would have worked but  
<sup>186</sup> could not provide the level of sensitivity required to confirm detection for neutrino cross  
<sup>187</sup> sections below  $10^{-39} \text{ cm}^2/\text{proton}$ . This was due to background interactions that came in  
<sup>188</sup> time directly from the bomb.

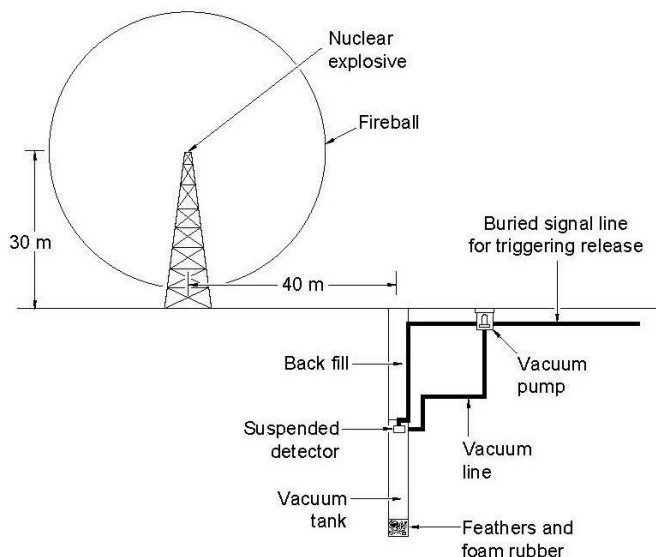
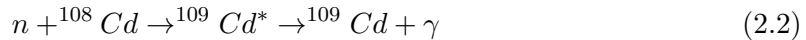


Figure 2.1: Original sketch of Cowan and Reines first proposed neutrino experiment.

Later, Reines realized tagging both the positron and neutron through a double coincidence would drastically reduce the backgrounds. This meant they could use a less intense neutrino source such as a nuclear reactor. They chose the Savannah River Plant near Augusta, Georgia which was estimated to produce neutrino fluxes on the order of  $10^{12} - 10^{13}$  neutrinos/s/cm<sup>2</sup>. The detector was composed of a water target that was doped with CdCl<sub>2</sub>. As stated prior, the signal would rely on a double coincidence flash measured from photomultipiler tubes inside their detector. First, they would detect the positron as it annihilates with an electron via pair production ( $e^+ + e^- \rightarrow \gamma + \gamma$ ). This is identified by two, back-to-back, coincident 0.511 MeV photons. Then, approximately 5  $\mu$ s later, a secondary photon would be detected which was produced from the neutron capture on Cadmium as shown in equation 2.2.



In 1956, only 25 years after Pauli's initial proposal of the neutrino, Cowan and Reines succeeded and provided the first direct experimental evidence of the electron flavor neutrino. In the subsequent years, the existence of two other flavors of neutrinos have been verified. In 1962, Lederman, Schwartz, and Steinberger discovered the  $\nu_\mu$  at Brookhaven National Laboratory by measuring neutrinos coming from pion decay. The  $\nu_\mu$  would be distinctly different from that of  $\nu_e$  if the process  $\nu_\mu + n \rightarrow p + e^-$  was forbidden. The results showed that the neutrinos from pion decay were indeed muon-like. Finally in 2000, the DONUT (Direct Observation of NeUtrino Tau) experiment stationed at Fermilab, made the first observed measurement of the  $\nu_\tau$ .

In 1956, C.S. Wu had shown that outgoing electron from beta decay maintained an opposing spin with respect to the spin of the parent nucleus. This turned out to be the first proof of maximal parity violation in weak interactions. Shortly thereafter, the neutrino helicity was first measured at Brookhaven National Labs by Maurice Goldhaber. In nature, neutrinos only have left handed helicity, while anti-neutrinos have right handed helicity. Helicity is frame dependent for particles with mass, which means there can be a reference frame in which the momentum vector can switch but the spin vector will not. For a

216 mass zero particles, this is not possible because the particle would already be traveling at  
217 the speed of light. This assumption is what lead to the believe that neutrinos were massless.

218 The number of active light neutrinos are well constrained by studying the decay of the  
219  $Z^0$  boson at LEP (Large Electron-Positron collider). LEP was an electron-positron collider  
220 ring with a circumference of approximately 27 km that supported four primary experiments  
221 (L3, ALEPH, OPAL and DELPHI). The facility was coined the phrase “Z-Factory” due  
222 to it’s ability to record approximately 1000  $Z^0$  boson decays every hour during optimal  
223 running conditions. The number of active neutrinos,  $N_\nu$  is related to the width of the  $Z^0$   
224 resonance. Using 17 million  $Z^0$  decays, LEP was able to show that  $N_\nu = 2.9840 \pm 0.0082$

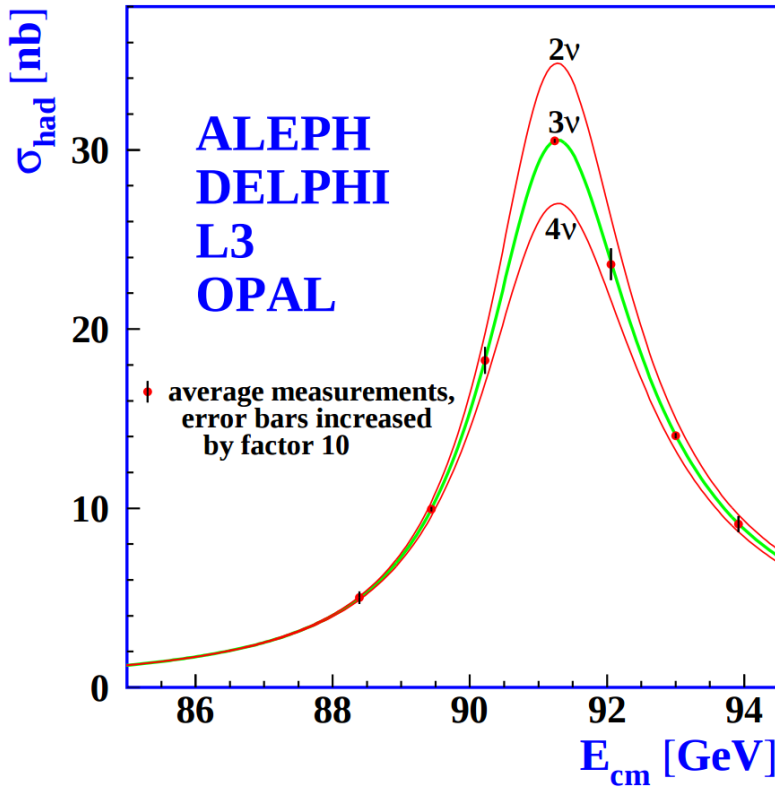


Figure 2.2: The Hadron production cross section around the  $Z^0$  resonance from LEP. The curves for two, three, and four neutrino flavors are shown. The fit shows very compelling evidence of three active flavors of neutrinos.

## 225 2.3 Neutrinos in the Standard Model

226 In the later half of the 20th century, scientists were looking for a way to describe all the  
227 fundamental forces and classify the known particles. The standard model of particle physics  
228 is a phenomenological framework that describes the interaction of fundamental particles be-  
229 tween the strong and electroweak forces. Having stood the test of time, the standard model  
230 accurately predicts most elementary particle interactions, but, does have it's limitations.  
231 The standard model does not account for gravity nor does it account for many new physics  
232 issues such as dark matter or dark energy. Most importantly, as we will see in section 2.5,  
233 it does not provide an accurate description of the neutrino.

234 The standard model consists of two types of particles, bosons and fermions. The funda-  
235 mental bosons consist of two families: gauge bosons, which are typically the force carriers,  
236 and scalar bosons, which refer to spin zero particles or fields. The gluon, photon, and the  
237 weak boson are gauge bosons that mediate the strong, electromagnetic, and weak forces, re-  
238 spectively. The Higgs boson is a scalar boson that possesses a nonzero vacuum expectation  
239 value of  $246\text{GeV}$ . This provides a mechanism for certain particles to gain mass even though  
240 their symmetries would suggest zero mass. The fundamental fermions are also divided  
241 into two families, quarks and leptons each having three generations. The quarks compose  
242 two main categories of particles, baryons and mesons. Baryons consist of an ensemble of  
243 3 quarks. The most common and stable baryons in the universe are protons ( $uud$ ) and  
244 neutrons ( $udd$ ). Meson consist of an ensemble of quark anti-quark pairs and tend to have  
245 shorter lifetimes than their corresponding baryons. The lightest and most common mesons  
246 are pions ( $u\bar{d}, d\bar{u}, u\bar{u}/d\bar{d}$ ) and kaons ( $u\bar{s}, s\bar{u}, d\bar{s}/s\bar{d}$ ). The leptons are also divided into two  
247 families with three generations each. The charged leptons, most notably the electron, inter-  
248 act via the electromagnetic and weak nuclear force and combine with nuclei to form stable  
249 baryonic matter. The neutral leptons are the neutrinos and only interact via the weak  
250 nuclear force. More details such as mass, charge, and spin for various particles are shown  
251 in figure 2.3

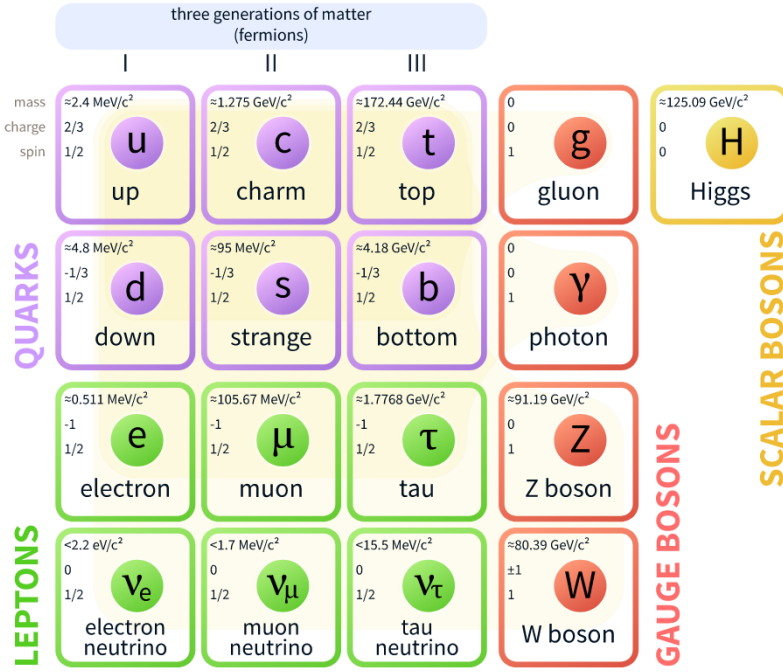


Figure 2.3: The current view of the standard model.

## 2.4 Neutrino Interactions

Neutrinos interact via the weak force. In the standard model, the weak force is unified with the electromagnetic force through an  $SU(2) \otimes U(1)$  symmetry. The structure of the  $SU(2)$  group symmetry accounts for the chirality of the fermion fields, along with ability to produce massive gauge bosons. The  $U(1)$  group symmetry accounts for the massless photon propagator needed for electromagnetic interactions. For the quark and fermion families we define fermion fields in equations 2.3 and 2.4 , respectively. For formality we will define right(left)- handed neutrino(anti-neutrino) fields knowing that they will become irrelevant as the theory evolves:

$$\psi_1(x) = \begin{pmatrix} q \\ q' \end{pmatrix}_L , \quad \psi_2 = q_R , \quad \psi_3 = q'_R \quad (2.3)$$

$$\psi_1(x) = \begin{pmatrix} \nu \\ l \end{pmatrix}_L , \quad \psi_2 = \nu_R , \quad \psi_3 = l_R \quad (2.4)$$

261 We begin with the free Lagrangian, defined in equation 2.5, as it is already invariant in  
262 flavor space.

$$\mathcal{L}_{\text{free}} \equiv \bar{\psi}(i\cancel{\partial} - m)\psi = i\bar{\psi}(x)\gamma^\mu\partial_\mu\psi(x) - m\bar{\psi}(x)\psi(x) \quad (2.5)$$

263 To make the Lagrangian invariant under local  $SU(2) \otimes U(1)$ , the fermion derivatives  
264 have to be changed to covariant objects. This produces 4 different gauge parameters, shown  
265 in equations 2.6, which correspond to the 4 different gauge fields required to describe the  
266  $W^\pm$ ,  $Z^0$ , and  $\gamma$ .

$$\begin{aligned} D_\mu\psi_1(x) &\equiv [\partial_\mu - ig\widetilde{W}_\mu(x) - ig'y_1B_\mu(x)]\psi_1(x) \\ D_\mu\psi_2(x) &\equiv [\partial_\mu - ig'y_2B_\mu(x)]\psi_2(x) \\ D_\mu\psi_3(x) &\equiv [\partial_\mu - ig'y_3B_\mu(x)]\psi_3(x) \end{aligned} \quad (2.6)$$

267 where,  $\sigma^i$  are the Pauli spin matrices and  $B_\mu$  represents a field imposed by an external  
268 source. We find that,

$$\begin{aligned} \widetilde{W}_\mu(x) &\equiv \frac{\sigma_i}{2} \left\{ \partial_\mu W_\nu^i - \partial_\nu^i + g\epsilon^{ijk}W_\mu^jW_\nu^k \right\} \\ B_{\mu\nu} &\equiv \partial_\mu B_\nu - \partial_\nu B_\mu \end{aligned} \quad (2.7)$$

269 The Lagrangian now satisfies  $SU(2) \otimes U(1)$  symmetry between all gauge fields as shown  
270 in equation 2.8. It should be noted that the fermion fields and gauge bosons are required to  
271 be massless. This does not accurately describe the true interaction since 3 of the 4 gauge  
272 bosons are known to have mass, but the theory does allow an interface between neutrino  
273 interactions in the standard model.

$$\mathcal{L} = \sum_{j=0}^3 i\bar{\psi}_j(x)\gamma^\mu D_\mu\psi_j(x) \quad (2.8)$$

274 From equation 2.8, the terms that account for interaction of gauge bosons with the  
275 fermion fields are shown below in equation 2.9

$$\mathcal{L} \rightarrow g\bar{\psi}_1(x)\gamma^\mu\widetilde{W}_\mu\psi_1(x) + g'B_\mu \sum_{j=0}^3 y_j\bar{\psi}_j(x)\gamma^\mu\psi_j(x) \quad (2.9)$$

276 From this, we are then able to construct the Lagrangian for both the charged and neutral  
 277 currents. The charge current Lagrangian is shown in equation 2.10.

$$\mathcal{L}_{CC} = \frac{g}{2\sqrt{2}} \left\{ W_\mu^\dagger [\bar{q}\gamma^\mu(1-\gamma_5)q' + \bar{\nu}\gamma^\mu(1-\gamma_5)\bar{l}] + \dots \right\} \quad (2.10)$$

278 The neutral current term in the Lagrangian contains gauge fields for both the Z boson  
 279 and photon, which can be broken into two terms to account for a non-zero Z boson mass  
 280 while leaving the photon massless through spontaneous symmetry breaking (SSB). This is  
 281 done through an arbitrary rotation, as shown in equation 2.11, where  $\theta_w$  is known as the  
 282 Weinberg or weak mixing angle. This angle is important because it is the angle used to  
 283 rotate through SSB giving the Z boson its mass.

$$\begin{pmatrix} W_\mu^3 \\ B_\mu \end{pmatrix} = \begin{pmatrix} \cos\theta_w & \sin\theta_w \\ -\sin\theta_w & \cos\theta_w \end{pmatrix} \times \begin{pmatrix} Z_\mu \\ A_\mu \end{pmatrix} \quad (2.11)$$

284 It is then possible to write the neutral current Lagrangian that accounts for the inter-  
 285 action of the Z boson as shown in equation 2.13.

$$\mathcal{L}_{NC} = \frac{e}{2\sin(\theta_w)\cos(\theta_w)} Z_\mu \sum_f \bar{f}\gamma^\mu(v_f - \alpha_f\gamma_5)f \quad (2.12)$$

286 where,

$$g\sin(\theta_w) = g'\cos(\theta_w) = e \quad \text{and} \quad \cos(\theta_w) = \frac{M_w}{M_z} \quad (2.13)$$

287 The neutral current coupling constants,  $v_f$  &  $\alpha_f$ , differ with respect to the various  
 288 quark, charged and neutral lepton fields. The neutrinos can be described as interactions via  
 289 the charged and neutral currents. The Feynman diagrams, shown in figure 2.4, depict how  
 290 the leptons couple to the quarks via the current mediator.

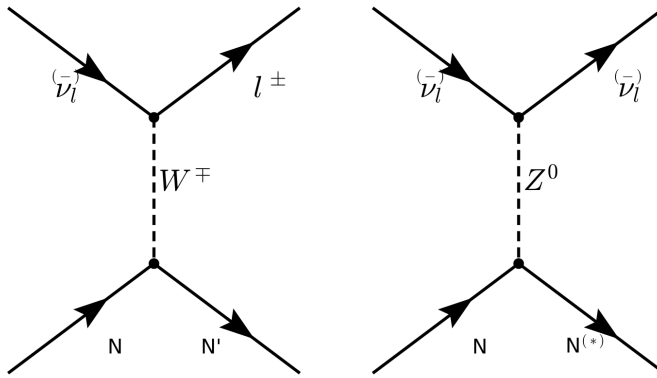


Figure 2.4: The Feynman diagram on the left describes a charged current (CC) neutrino interaction which transforms neutrinos into their corresponding charged leptons. In the CC interaction diagram the  $N \rightarrow N'$  represents a changed nucleon charge. The diagram on the right shows the neutral current(NC) neutrino interaction with preserves the neutrino while it interacts. In the NC interaction diagram the  $N \rightarrow N^*$  represents a same charge nucleon that could be at a higher resonance state.

## 2.5 Neutrino Mass and Flavor Oscillations

Neutrino oscillation is a quantum mechanical phenomenon in which the fraction of neutrino flavor changes while it propagates. This phenomena was first proposed in 1957 by Bruno Pontecorvo and relates the neutrino mass eigenstates with the flavor eigenstates through a rotation. This phenomena is best shown through a two neutrino flavor example, then extended into 3 flavors.

The mixing matrix for a two flavor neutrino case is:

$$\begin{pmatrix} \nu_e \\ \nu_\mu \end{pmatrix} = \begin{pmatrix} \cos \theta & \sin \theta \\ -\sin \theta & \cos \theta \end{pmatrix} \begin{pmatrix} \nu_1 \\ \nu_2 \end{pmatrix} \quad (2.14)$$

In this example, the flavor states are represented as  $\nu_e$  and  $\nu_\mu$  which are expressed as a mixture of mass states  $\nu_1$  and  $\nu_2$ . For aesthetic reasons, we chose  $\nu_\mu$  to be part of the example because most man made neutrino beams produce a relative pure sample of  $\nu_\mu$ . The framework for this example is commonly used as an oscillation approximation and can be generalized to satisfy any case of two distinctly different flavor neutrinos.

303 Using the two flavor formalism a pure  $\nu_\mu$  neutrino state can be expressed as equation  
 304 2.15

$$|\nu_\mu(0)\rangle = -\sin \theta |\nu_1(0)\rangle + \cos \theta |\nu_2(0)\rangle \quad (2.15)$$

305 The evolution of the state is governed by solving the time dependent Schröedinger  
 306 equation for the initial muon state:

$$|\nu_\mu(t)\rangle = e^{-i\frac{Et}{\hbar}} |\psi(0)\rangle = -e^{-i\frac{E_1 t}{\hbar}} \sin \theta |\nu_1\rangle + e^{-i\frac{E_2 t}{\hbar}} \cos \theta |\nu_2\rangle \quad (2.16)$$

307 Assuming neutrinos travel near the speed of light, we rewrite equation 2.16 using the  
 308 relativistic approximation, along with setting  $c = \hbar = 1$  and  $p_1 = p_2 = p$ :

$$|\nu_\mu(t)\rangle \simeq -e^{-i(p_1 + \frac{m_1^2}{2p_1})t} \sin \theta |\nu_1\rangle + e^{-i(p_2 + \frac{m_2^2}{2p_2})t} \cos \theta |\nu_2\rangle \quad (2.17)$$

309 with,

$$E = \sqrt{p^2 + m^2} = p \sqrt{1 + \frac{m^2}{p^2}} \approx p + \frac{m^2}{2p} \quad (2.18)$$

310 Next, the mass terms are grouped together and defined as the absolute square difference,  
 311  $\Delta m^2 \equiv |m_2^2 - m_1^2|$ . We find that if the mass are different then the mass eigenstates propagate  
 312 at different frequencies and give rise the oscillatory behavior. The time dependent state can  
 313 now be wrote as:

$$|\nu_\mu(t)\rangle = e^{-i\phi} (-\sin \theta |\nu_1\rangle + e^{+i\frac{\Delta m^2}{2p}t} \cos \theta |\nu_2\rangle) \quad (2.19)$$

with,  $e^{-i\phi} \equiv e^{-i\left(p + \frac{m_1}{2p}\right)t}$

314 To calculate the probability of the initial  $\nu_\mu$  state being measured as a  $\nu_e$  state at some  
 315 later time  $t$ , we need to calculate the absolute value squared of the overlap between the  
 316 states. Utilizing the relationship  $\langle \psi_i | \psi_j \rangle = \delta_{ij}$ , the overlap between the states is:

$$\langle \nu_e | \nu_\mu(t) \rangle = e^{-i\phi} (-\sin \theta \cos \theta + \sin \theta \cos \theta e^{i\frac{\Delta m^2}{2p}t}) \quad (2.20)$$

<sup>317</sup> The probability reduces to:

$$\begin{aligned}
 P(\nu_\mu \rightarrow \nu_e) &= |\langle \nu_e | \nu_\mu(t) \rangle|^2 \\
 &= e^{i\phi} e^{-i\phi} \sin^2 \theta \cos^2 \theta (-1 + e^{-i\frac{\Delta m^2}{p}t})(-1 + e^{+i\frac{\Delta m^2}{p}t}) \\
 &= \frac{1}{2} \sin^2 2\theta \left( 1 - \cos \left( \frac{\Delta m^2}{2p} t \right) \right)
 \end{aligned} \tag{2.21}$$

<sup>318</sup> Finally, from relativistic assumptions, we set  $p = E_\nu$  as the outgoing neutrino energy  
<sup>319</sup> and  $t = L$  corresponds to the distance traveled.

$$P(\nu_\mu \rightarrow \nu_e) = \sin^2 2\theta \sin^2 \left( \frac{\Delta m^2 L}{4E_\nu} \right) \tag{2.22}$$

<sup>320</sup> From a proper accounting of numerical values of  $c$  and  $\hbar$ , equation 2.26 is more com-  
<sup>321</sup> monly written as:

$$P(\nu_\mu \rightarrow \nu_e) = \sin^2 2\theta \sin^2 \left( 1.27 \frac{\Delta m^2 L}{E_\nu} \right) \tag{2.23}$$

<sup>322</sup> This oscillation behavior is best visualized as a plot of the probability of appearance  
<sup>323</sup> and disappearance as shown Figure 2.5.

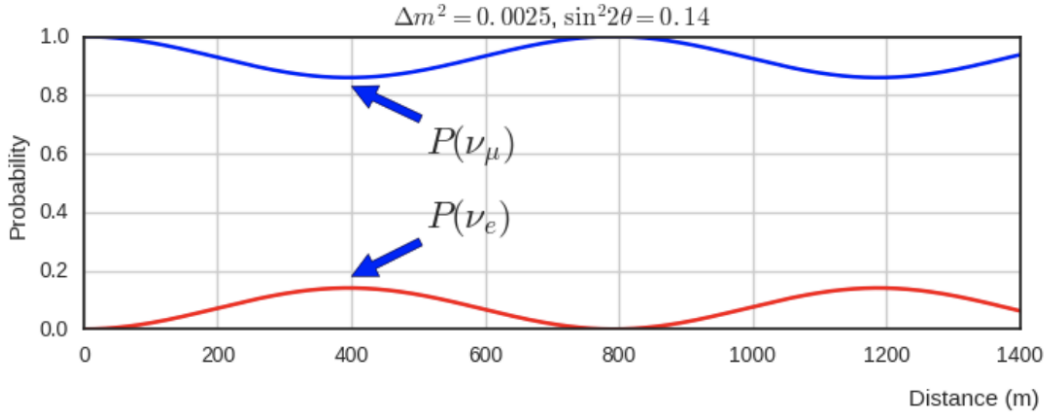


Figure 2.5: This plot shows the appearance and disappearance curves for a 2-flavor approximation as a function of baseline. The values of  $\Delta m^2 = 0.0025 \text{ eV}^2$  and  $\sin^2 \theta = 0.14$  are used.

324 As shown prior from figure 2.2, there are very good constraints on the number of active  
 325 neutrinos[3]. Extending this formalism to a 3 flavor case was done by Pontecorvo-Maki-  
 326 Nakagawa-Sakata (PMNS). The PMNS matrix is a 3 dimensional unitary matrix which  
 327 is parameterized by three mixing angles  $\theta_{12}, \theta_{23}, \theta_{13}$  a complex phase  $\delta$ . The three angle  
 328 correspond to the mixing effect, while  $\delta$  is known as the charge parity (CP) phase. If the  
 329 CP-phase is non-zero, then neutrinos violate charge parity conservation which leads to the  
 330 conclusion that neutrinos and anti-neutrinos interact differently with matter. The value for  
 331  $\delta$  has yet to be observed.

$$U_{PMNS} = \begin{pmatrix} 1 & 0 & 0 \\ 0 & c(\theta_{23}) & s(\theta_{23}) \\ 0 & -s(\theta_{23}) & c(\theta_{23}) \end{pmatrix} \begin{pmatrix} c(\theta_{13}) & 0 & s(\theta_{13})e^{-i\delta} \\ 0 & 1 & 0 \\ -s(\theta_{13})e^{i\delta} & 0 & c(\theta_{13}) \end{pmatrix} \begin{pmatrix} c(\theta_{12}) & s(\theta_{12}) & 0 \\ -s(\theta_{12}) & c(\theta_{12}) & 0 \\ 0 & 0 & 1 \end{pmatrix} \quad (2.24)$$

332 where  $c(\theta_{ij}) \equiv \cos \theta_{ij}$  and  $s(\theta_{ij}) \equiv \sin \theta_{ij}$ . The matrix equation is now put into a more  
 333 compact manor that relates the mixing of the 3 neutrino generations.

$$\begin{pmatrix} \nu_e \\ \nu_\mu \\ \nu_\tau \end{pmatrix} = \begin{pmatrix} U_{e,1} & U_{e,2} & U_{e,3} \\ U_{\mu,1} & U_{\mu,2} & U_{\mu,3} \\ U_{\tau,1} & U_{\tau,2} & U_{\tau,3} \end{pmatrix} \begin{pmatrix} \nu_1 \\ \nu_2 \\ \nu_3 \end{pmatrix} \quad (2.25)$$

334 In it's most general form, the oscillation probability is:

$$P(\nu_\alpha \rightarrow \nu_\beta) = \delta_{\alpha,\beta} - 4 \sum_{j>i} U_{\alpha,i} U_{\beta,j} U_{\alpha,j}^* U_{\beta,j}^* \sin^2 \left( 1.27 \frac{\Delta m_{ij}^2 L}{E_\nu} \right) \quad (2.26)$$

335 From equation 2.26, we see that the oscillation probability is depended on the mass  
 336 difference between states. Currently, there are no successful direct measurements of any  
 337 given neutrino mass state. Therefore, there is an allowed ambiguity in the mass ordering  
 338 of all three neutrino states. This is called the neutrino hierarchy problem. However, we do  
 339 know that the difference between  $m_1$  and  $m_2$  is small relative to  $m_3$ . Using this, we can  
 340 build a picture of the fraction of different flavor eigenstates corresponding to their various  
 341 mass states for both types of hierarchy.

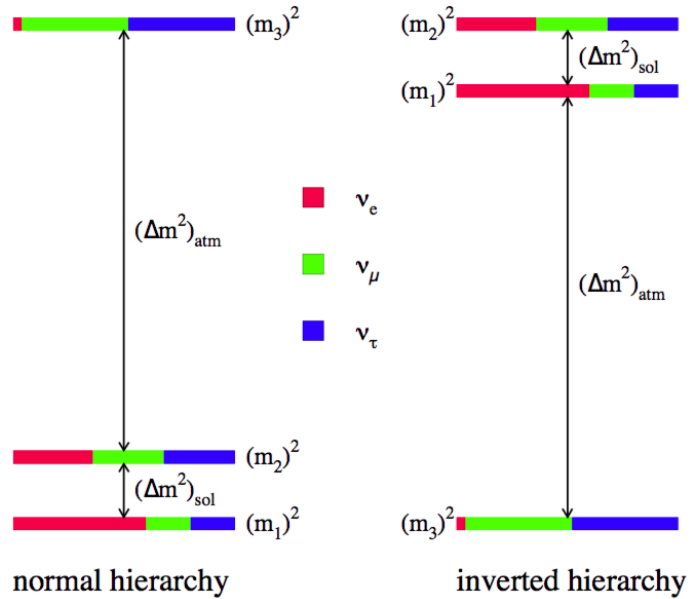


Figure 2.6: The two possible ordering for the 3 active neutrino mass eigenstates.

Many experiments have measured various elements of the PMNS matrix with neutrinos coming from accelerators, reactors, and solar sources. Currently, normal hierarchy ( $m_1 < m_2 < m_3$ ) is favored. Therefore, we will show (table 2.27) the current Particle Data Group (PDG)[4] best fit values for oscillation parameters with respect to normal hierarchy.

$$\begin{aligned}
\Delta m_{21}^2 &= 7.37 \times 10^{-5} eV^2 \\
\Delta m_{32}^2 &= 2.50 \times 10^{-3} eV^2 \\
\sin(\theta_{12}) &= 0.297 \\
\sin(\theta_{23}) &= 0.437 \\
\sin(\theta_{13}) &= 0.0214 \\
\delta/4 &= 1.35
\end{aligned} \tag{2.27}$$

## <sup>346</sup> 2.6 Sterile Neutrinos

<sup>347</sup> It is well accepted, from measurements at LEP[5], that there are only 3 neutrinos that couple  
<sup>348</sup> through the weak interaction. Mathematically, nothing prohibits a theory that allows for  
<sup>349</sup> neutrino mixing with other neutrino states beyond the 3 active states. These states, since  
<sup>350</sup> they do not interact weakly, are called 'sterile neutrinos'. Extending the 3 flavor oscillation  
<sup>351</sup> model to include any number of sterile neutrinos may be a possibility to address some the  
<sup>352</sup> currently unexplained results in the neutrino physics fields. Each additional state requires  
<sup>353</sup> an extra dimension to be added to the PMNS matrix. The sterile eigenstates are then  
<sup>354</sup> defined as

$$|\nu_{s_i}\rangle = \sum_j^{3+N} U_{s_i,j} |\nu_j\rangle \quad (2.28)$$

<sup>355</sup> where N is the number of sterile neutrinos. The necessity for additional sterile neutrinos  
<sup>356</sup> was prompted by the LSND experiment and later supported by the MiniBooNE. experiment.  
<sup>357</sup> Both experiments are explained in depth in chapter 5. Each experiment found an excess  
<sup>358</sup> of electron-like events at low energy. This suggested a  $\Delta m^2$  parameter space observed to  
<sup>359</sup> be  $1\text{eV}^2$  larger than expected and strongly contradicted the results of many other results  
<sup>360</sup> which had  $\Delta m^2$  around  $\mathcal{O}(10^{-3}\text{eV}^2)$  and  $\mathcal{O}(10^{-5}\text{eV}^2)$ . This precipitated the need for  
<sup>361</sup> further exploration of the LSND and MiniBooNE claims with more sophisticated detector  
<sup>362</sup> technologies. The MicroBooNE experiment was proposed in 2001 and will be the focal point  
<sup>363</sup> for this thesis.

## 364 Chapter 3

# 365 The MicroBooNE Detector

### 366 3.1 Brief History of LAr-TPC's

367 The surprising nature of neutrinos quickly prompted the need for precision measurements  
368 of their interactions. Unfortunately, the low neutrino cross section posed a hurdle to build a  
369 high statistics detector. In 1977, C.Rubbia propose a Liquid Argon Time Projection Cham-  
370 ber (LArTPC) as large, high precision neutrino detector.[6] In 2001, The ICARUS collabo-  
371 ration commissioned the T600 detector which was one of the first large scale LArTPC's to  
372 be used as a neutrino detector. [7] The T600, which is comprised 760 tons of liquid argon  
373 and commissioned in Pavia, Italy using cosmic rays as a proof of principle. Later the T600  
374 was place underground in Hall B of Laboratori Nazionali del Gran Sasso (LNGS) which is  
375 located 730 km from the source of the CERN neutrino beam.

376 In 2009, the AgroNeut collaboration, commissioned a small LArTPC in a 175 liter  
377 vacuum jacketed cryostat. The ArgoNeut TPC was comprised of 3 wire planes and operated  
378 at a drift field of 500 V/cm. The detector was placed just in front of the MINOS near  
379 detector in the NuMI beam at Fermi National Accelerator Laboratory (FNAL)[8]. AgroNeut  
380 collected thousands of neutrino and antineutrino events providing valuable physics data and  
381 detector R&D for future experiments with LArTPC's.

382 The MicroBooNE (the Micro Booster Neutrino Experiment) detector, which will be  
383 discussed in depth throughout this chapter, is the first multi-ton LArTPC to be fully oper-  
384 ational in the U.S.[9] The MircoBooNE detector design pioneered many new detector R&D

concepts such as: the ability to maintain high LAr purity in an unevaluated vessel, implementation of low noise electronic readouts at liquid cryogenic temperatures and advances in reconstruction techniques. MicroBooNE also supports a robust, high statistics physics program to address the MiniBooNE Low Energy Excess and various cross section measurements. MicroBooNE was commissioned and began taking cosmic ray data in the summer of 2015. In October 2015 it began taking neutrino data. Shortly there after, the first neutrino event candidates were identified. [10]

### 3.2 Introduction

The MicroBooNE detector utilizes 170 tons of liquid argon to sustain 87 tons of active detector mass.[11] It is located at the Liquid Argon Test Facility (LArTF) which is 470 m downstream of the Booster Neutrino Beamline (BNB) source at the Fermilab National Accelerator Lab (FNAL) in Batavia, Illinois. The detector is the first large scale LArTPC to be deployed, commissioned and fully operated in the U.S.

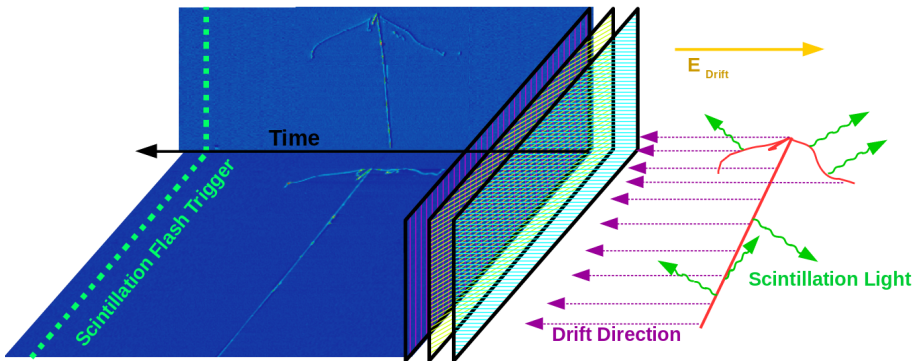


Figure 3.1: This diagram illustrates how a TPC works. First, charged tracks ionize the argon. The ions produce prompt scintillation light and the corresponding electrons begin to drift towards the wires due to the presence of the electric field. When the drift electrons reach the wire planes a 2D image is produced for each plane. When combining the 2D images from multiple planes along with the scintillation light information a 3D reconstruction is possible.

The general principle of a LArTPC involves utilizing two properties of LAr, scintillation

399 light and ionization. Charged particles travel through the argon and produce scintillation  
400 light which is collected by photomultiplier tubes (PMT's). A uniform electric field is applied  
401 over active volume which transports the ionization electrons to a series of wire planes.  
402 Assuming the argon is pure and has minimal electro-negative contaminants, the wire planes  
403 then measure the induced or collected charge signal from the drifting electrons. The planes  
404 are each oriented at a different pitch angles. Each plane then can then produce a two  
405 dimensional image of the event as a function of wire and time. Combining multiple planes  
406 along with the PMT information allows for the object to be fully reconstructed in three  
407 dimensions. A diagram of the TPC concept is show in Figure 3.1. In the following sections  
408 the TPC, light collection system, and electronics are described in detail.

### 409 **3.3 Time Projection Chamber**

410 The TPC is the core of the MicroBooNE detector and forms a rectangular prism with  
411 dimensions  $2.3\text{ m} \times 2.6\text{ m} \times 10.4\text{ m}$  which contains 87t of LAr. The longest dimension,  
412 which in MicroBooNE's coordinate system is refereed to as the z-direction, is oriented on  
413 axis of the BNB. The majority of the TPC materials are composed of 304V stainless steel  
414 and G10. Stainless steel was chosen due to it's low magnetic susceptibility, resistance to  
415 corrosion/oxidation, and ability to maintain it's strength in cryogenic temperatures. G10  
416 was chosen due to it's ability to perform well as an insulator in cryogenic environments.



Figure 3.2: The MicroBooNE TPC is shown here. On the far right is the flat cathode plane. The far left shows the 8,456 anode wires installed. The field cage tubes, which provide the uniform electric field, span the length between the anode and cathode.

417     The TPC field cage, which provides the uniform electric field through the detector  
 418     volume, and was designed to produce field strengths up to 500 v/cm in liquid argon. The  
 419     field cage consists of a total of 64 stainless steel rectangular loops that are supported and  
 420     evenly spaced by a G10 holder. The cathode plane is a series flat stainless steel sheets that  
 421     is opposite the anode sense wires. Figure 3.2 shows the MicroBooNE TPC.

422     Every piece that was used in the MicroBooNE detector was thoroughly cleaned. Many  
 423     pieces were cleaned in an ultrasonic cleansing bath while others were cleaned by hand.  
 424     The detector was constructed in a clean environment that maintained positive pressure to  
 425     mitigate the accumulation of dust. A complete description of the process is summarize in  
 426     a separate technical note. [12]

427     MicroBooNE has a total of 8,265 sense wires that form 3 unique wire planes, one vertical  
 428     collection plane (Y) and two induction planes ( U,V ) oriented at  $\pm 60$  relative the Y plane.  
 429     The wire planes are separated by 3 mm. The wires in each plane are evenly spaced by 3  
 430     mm pitch on carrier boards. The Y plane consists of 3,456 wires with a total of 108 carrier  
 431     boards that accommodate 32 wires each. Each of the U and V planes consist of 2,400 wires  
 432     with a total of 150 carrier boards that accommodate 16 wires each. The wires themselves  
 433     are made of 304V stainless steel and are  $150 \pm 5 \mu\text{m}$  in diameter. A  $2\mu\text{m}$  layer of copper  
 434     is plated over the wires to decrease the resistivity from  $40 \Omega/\text{m}$  to  $3 \Omega/\text{m}$ . The reduced

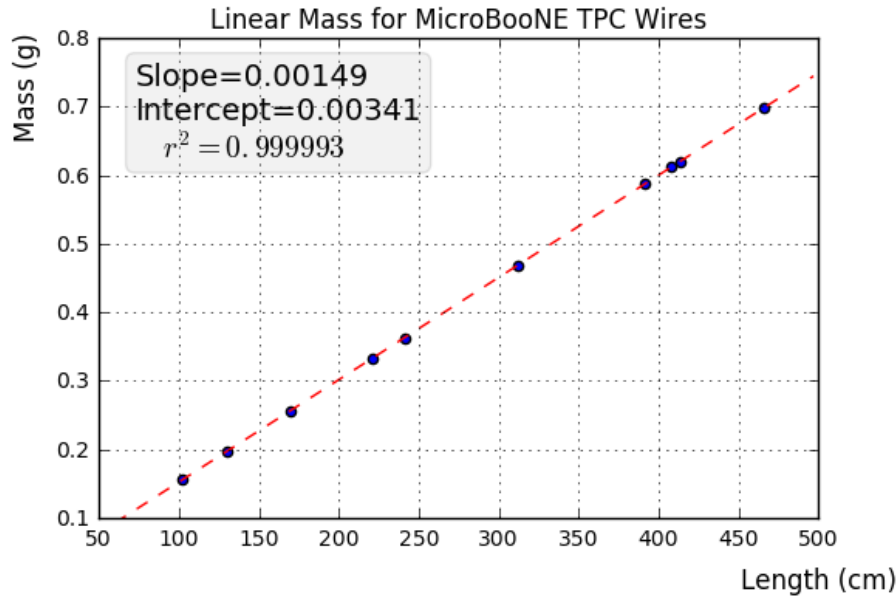


Figure 3.3: This plot is for a small sample used to cross check the linear mass density measured from the wire dealer. The slope from this plot represents the linear mass density and was found to be consistent with the value  $0.149\text{g/m}$

435 resistivity aids in noise reduction at cryogen temperatures. Finally the wire is covered in  
 436 and outer layer  $0.1\mu\text{m}$  of gold to prevent the copper from oxidizing over time. The linear  
 437 mass density of a small sample of wires was measured and is shown in figure 3.3.

438 The wires were designed to installed at a nominal tension of 6.97 N. To account for this,  
 439 the carrier boards were installed onto a series of tensioning bars on the anode frame. These  
 440 tensioning system, as shown in figure 3.4, allowed for fine tune adjustments to be made to  
 441 separate sections of wires.

442 There are a total of 12 tensioning bars, 2 sets of 5 that traverse the entire top and bottom  
 443 length of the anode frame, and 2 spanning the entire height of the upstream and downstream  
 444 sections of the anode frame. Bronze jacking screws were used for final adjustments once  
 445 all the wires were installed. Bronze was chosen since it has a similar thermal expansion  
 446 coefficient to stainless steel and it is a softer metal which helps mitigate the risk of cold  
 447 welding with stainless steel during the tensioning process.

448 In preparation for installing the actual detector wires, an installation team was trained

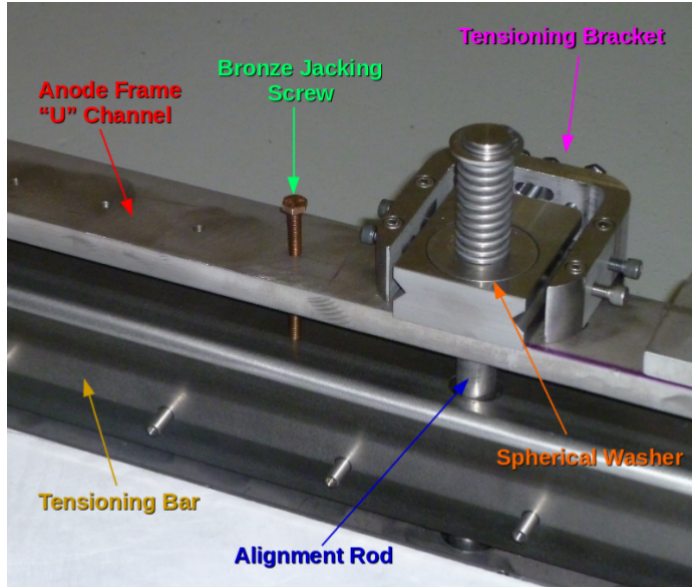


Figure 3.4: The MicroBooNE tension system. Wire carrier boards (not shown here) are mounted on the tensioning bar. The tensioning bar is able to move the wires during the tensioning process. Bronze jacking screws were used for final alignment during the tensioning process

449 on how to properly handle and install them. A 'mock-wire' installation was done to practice  
 450 and identify the risks. After this, the actual wires were installed. The installation took  
 451 approximately one week. The wires were installed serially, first the Y-plane, then the U-  
 452 plane, and then the V-plane. After all the wires were install, a G10 cover board was placed  
 453 over carrier boards to secure and protect the electronics on the board, as shown in figure  
 454 3.5.

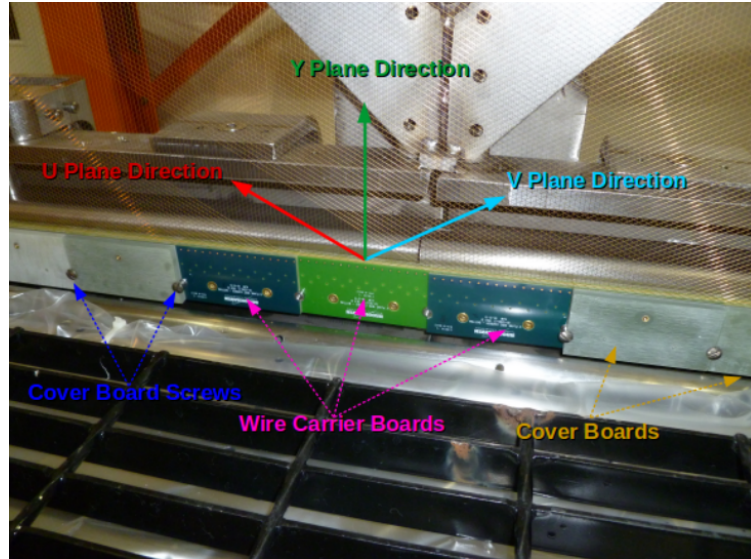


Figure 3.5: The MicroBooNE wires for 3 planes are shown here. The wire carrier boards are serially installed on the tensioning bar. The boards are held in place with a G10 cover plate that is secured with a smooth stainless steel screw.

455      Next, the wires were brought as close to nominal tension as possible. It was decided to  
 456      favor under tensioning wires to minimize the risk of a broken wire during the tensioning  
 457      process. The wire tensioning was done in a systematic way using the bronze jacking screws.

$$f = \frac{1}{2L} \sqrt{\frac{T}{\rho}} \quad (3.1)$$

458      Each wire has a characteristic resonance frequency that is related to its length, tension,  
 459      and linear mass density through equation 3.1. A custom device was made to measure  
 460      the resonant frequency of individual MicroBooNE wires. A laser light was focused on a  
 461      particular wire and the wire gently plucked. A photo-diode mounted in an optical lens then  
 462      measured the intensity of reflected light as the wire vibrated. The signals were then read into  
 463      SpectrumAnalyzer, which is a software package that records frequency. SpectrumAnalyzer  
 464      also allowed the high order frequency harmonics to be seen. The higher frequencies allowed  
 465      for more precise tension measurement as see in Figure 3.6

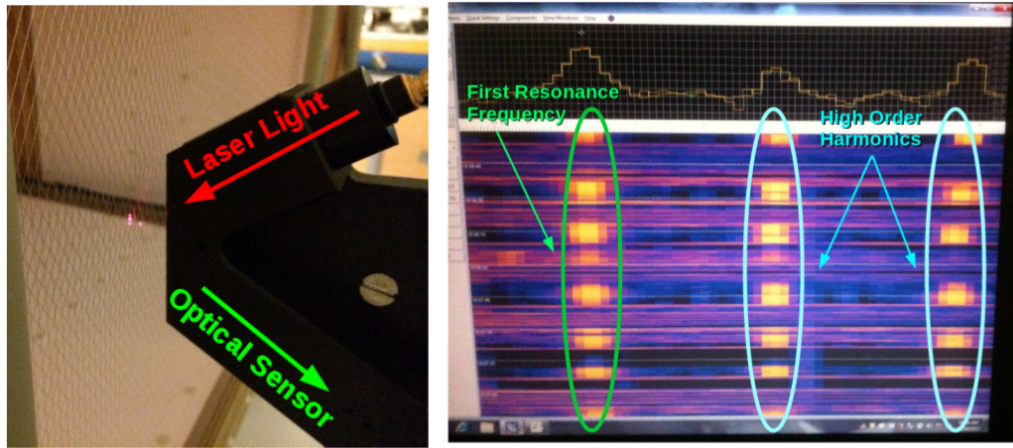


Figure 3.6: Left: Picture of the tension measuring apparatus including a laser and a optical sensor made of a photo-diode and a lens. Right: Example output of the SpectrumAnalyzer showing the first resonance frequency (bright line on the left) and the higher order harmonics (lines in the middle and left).

466 Note that the tension of 2328 out of 2400 U wires, 2308 out of 2400 V wires, and 3410  
 467 out of 3456 Y wires was measured, corresponding to 97.5 % of all wires installed in the  
 468 detector. Only the wires inaccessible to the tension measuring device were not measured.  
 469 The average tension for U,V,Y planes respectively was  $0.589 \pm 0.012$  kg,  $0.664 \pm 0.014$  kg,  
 470  $0.525 \pm 0.009$  kg. The tension for each plane is shown in Figure 3.7 and Figure 3.8.

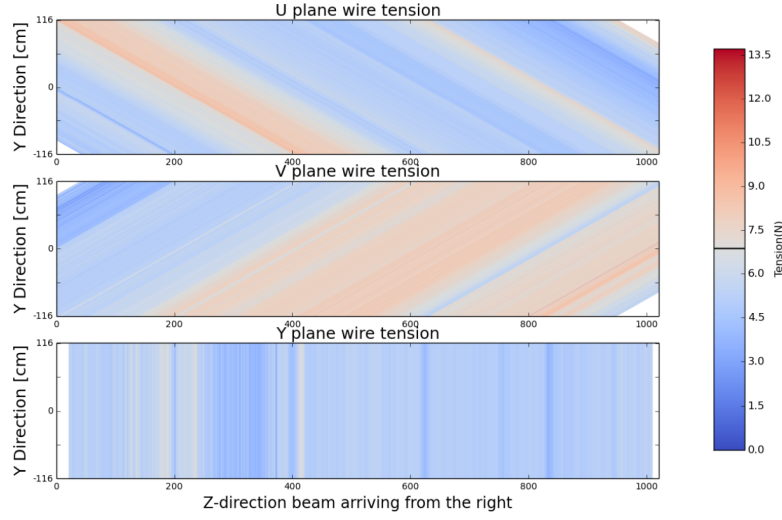


Figure 3.7: This a plane by plane map of the measured wire tensions for MicroBooNE.

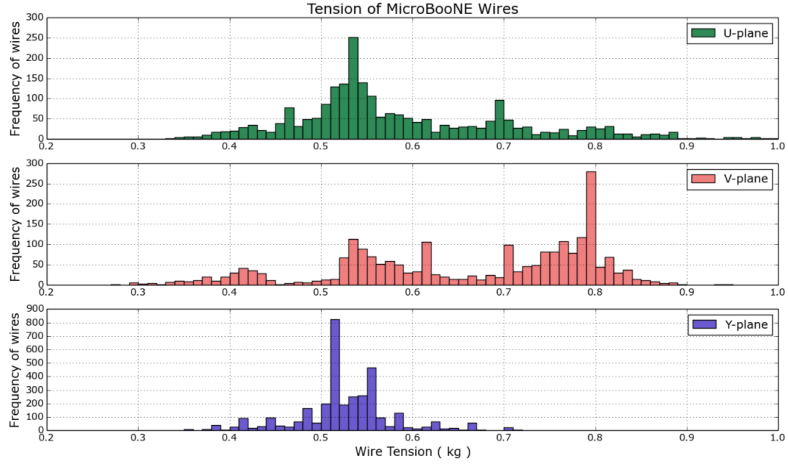


Figure 3.8: This a plane by plane histogram of the measured wire tensions for MicroBooNE.

### 471 3.4 Light Collection

472 The TPC can reconstruct 3D objects but there is still an ambiguity in the initial drift  
 473 position. The light collection system in an LArTPC provides information to address this  
 474 degeneracy. Scintillation light of liquid argon is 128nm wavelength and is produced through  
 475 two primary reactions. The first, which accounts for  $\approx 25\%$  of the light yield, is done  
 476 through a  $\Sigma$  singlet excimer excitation and has a reaction time of  $6 \pm 2$  ns. This type of

477 excimer is formed from an ionized argon atom that combines with another stable argon  
 478 atom. The second, which accounts for the other 75% of light yield, is done through a  $\Sigma$   
 479 triplet excimer excitation and has a reaction time of  $1590 \pm 100 \mu\text{s}$ . The triplet state excimer  
 480 is formed from a stable argon atom, an ionized argon atom, and a free electron. Since the  
 481 prompt scintillation light is orders of magnitude faster than drift time from the TPC signal  
 482 this information can be used to address this ambiguity.

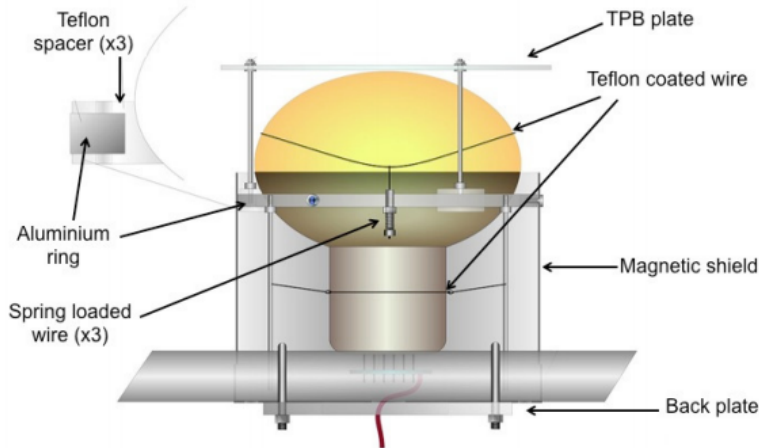


Figure 3.9: Schematic of a PMT optical unit for MicroBooNE.

483 The MicroBooNE light collection system consists of 32 8-inch diameter Hamamatsu  
 484 R5912-02mod cryogenic PMTs. The PMT's are not optimized to detect 128nm light. There-  
 485 fore, an acrylic plate coated with tetraphenyl butadiene (TPB)[13] was installed in front  
 486 of the PMT's to act as a wavelength shifter. The TPB plate absorbs the 128nm light and  
 487 re-emits it a peak wavelength of 425nm. Also, it is known that PMT response is reduced  
 488 from certain orientations in the earth magnetic field. To address this a mu-metal shield was  
 489 designed to extend just past the equator of the PMTs. A schematic of a PMT optical unit  
 490 is shown in figure 3.9.

491 The PMT system is mounted on a railing behind the wire planes and spans the entire  
 492 detector length as shown in figure 3.10. This also provides a weak handle on interaction  
 493 position since the scintillation light is fairly localized. Most importantly, since MicroBooNE  
 494 is a surface detector and constantly being bombarded by cosmic rays, the scintillation flash

495 is used as a method of identifying neutrino interactions coming in time with the beam.



Figure 3.10: PMT optical units installed on support racks inside the MicroBooNE cryostat

### 496 3.5 Electronics Readout

497 The TPC and PMT systems produce detector analog signals which need to be digitized,  
498 transferred out of the detector, and written to disk through data acquisition (DAQ) software.  
499 Both systems perform a first round of shaping and amplification in the cold LAr and then  
500 interface with warm electronics for further processing. The DAQ continuously writes to disk  
501 and creates a buffer which stores data for up to 24 hours. MicroBooNE employs various  
502 triggers to signify beam and non-beam data blocks and permanently store data from the  
503 buffer stream. A schematic overview of the TPC and PMT signal processing and readout  
504 stages is shown in Figure 3.11.

505 For the TPC, a large portion of the electronics processing for the 8,256 wire signals  
506 is performed directly in the LAr. To reduce electronics noise, the input distance from  
507 the wires to the preamplifier is minimized. The sense wires directly interface with CMOS  
508 analog front end ASICs which operate on cold motherboards. In total MicroBooNE has  
509 516 CMOS ASICs. The ASICs generate 50 W of heat load which is a negligible impact on  
510 the cryogenics system. The motherboards shape and amplify the low noise signal. There

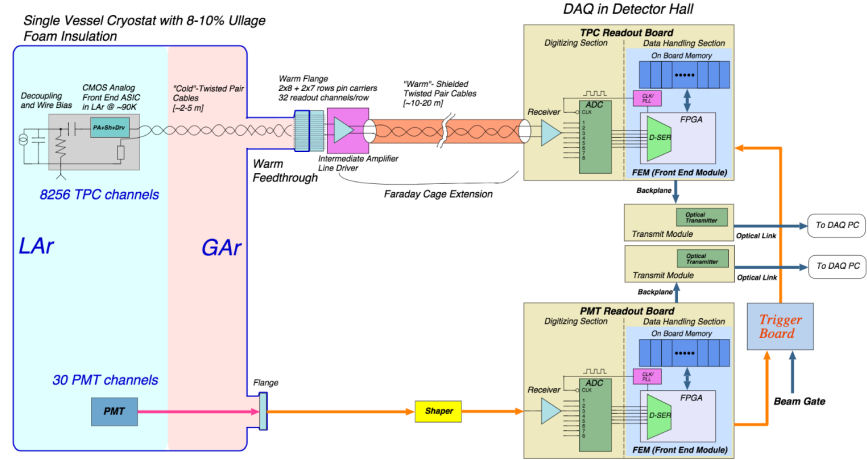


Figure 3.11: MicroBooNE LArTPC and PMT signal processing and readout schematic.

511 are 36 top style motherboards that instrument Y, U and V plane wires and 14 side style  
 512 motherboards that instrument U and V plane wires. The signals are then passed through a  
 513 series of 12 feedthrough ports to warm electronics. The warm signals are then distributed  
 514 over nine readout crates, which digitize the signals.

515 The TPC system read out frame is defined to be 1.6 ms. This number was chosen  
 516 to account for ionization electrons that are generated at the cathode and drift the entire  
 517 distance to the wires in the presence of a 500 V/cm E-Field. In MicroBooNE, an event  
 518 is defined as four 1.6 ms readout frames. The additional frames allow for identification of  
 519 cosmic particles that arrive before and after the neutrino interaction.

520 The PMT system is also processed in a similar fashion. The PMT's undergo 60 ns  
 521 shaping to allow for precise measurements of the signal rising edge. The signals are sampled  
 522 at 64MHz but only shaped signals above a threshold are read out and stored for data. The  
 523 PMT signals are split into two different gains. A high gain signal that is 10 times the  
 524 amplitude of the low gain. The signals are then brought to pre-amp/shaper boards and  
 525 digitized and sent to the DAQ.

## 526 Chapter 4

# 527 Booster Neutrino Beam

528 Fermilab is one of the world's leading neutrino facilities and currently produces two neutrino  
 529 beams that span a wide range of neutrino energies. The Booster Neutrino Beam (BNB),  
 530 which will be described in detail throughout this chapter, is a lower energy beam that  
 531 delivers neutrinos to various short baseline experiments. Fermilab also hosts the NuMI  
 532 (Neutrinos at the Main Injector) Beam which produces neutrinos over a large range between  
 533 1 GeV/c - 30 GeV/c and delivers neutrinos to various experiments both on-axis and off-axis.  
 534 The NuMI beam will not be covered in this thesis.

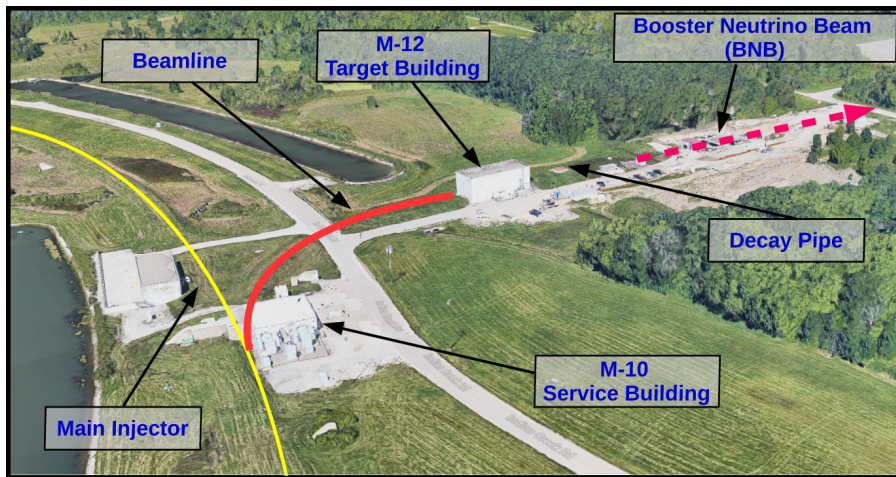


Figure 4.1: This image shows an aerial view of the Booster Neutrino Campus. Protons are extracted before the main injector near the M-10 service building and delivered to the M-12 target hall where the low energy neutrino beam is produced.

535        The Booster neutrino campus is illustrated in figure 4.1. To produce the BNB, pro-  
536        tons are extracted from a transfer line just prior to the main injector and then interact  
537        with a beryllium target. The following sections will describe the beam system, neutrinos  
538        production process, and flux predictions for the BNB.

## 539        4.1 Primary Beam, Target and Horn

540        The BNB extracts 8.89 GeV/c momentum protons from the Fermilab Booster synchrotron  
541        and delivers them to a Beryllium target housed in the M-12 building. The protons from  
542        the booster are grouped in  $1.6 \mu\text{s}$  windows called 'beam spills'. One beam spill contains  
543        approximately  $5 \times 10^{12}$  protons. On average the Booster can run no more than 5 Hz with  
544        no more than 11 pulses in a row at 15 Hz. In optimal running conditions the Booster can  
545        deliver  $9 \times 10^{16}$  protons on target (P.O.T) per hour.

546        The beam pipe directly leading to the target is approximately 5 feet long and is held  
547        under vacuum to minimize proton interactions not originating from the target. The incom-  
548        ing proton flux is measured by a pair of toroids which are positioned upstream of the target  
549        and provide an error on P.O.T on the order of 2%.

550        The target consists of 7 cylindrical Beryllium slugs that together produce an effective  
551        cylinder of 71.1 cm in length and 0.51 cm in radius. The use of multiple slugs gave the  
552        Beryllium more surface area to allow efficient heat transfer from a simple air cooling system  
553        to be sufficient. An exploded view of the BNB target is shown in figure 4.2. As the  
554        protons collide with the beryllium, large amounts of secondary and tertiary mesons, such  
555        as  $\pi^\pm$  and  $K^\pm$ , are produced. These mesons will later decay into neutrinos and other decay  
556        particles.

557        The target is positioned inside of a large toroidal electromagnet called a horn. The horn  
558        is made of an aluminum alloy (6061 T6) and is pulsed with 174 kA of current to produces  
559        a  $1/R$  field where R is the distance from the axis of the horn. Since neutrinos are neutral  
560        particles they cannot be directly focused by an electric or magnetic force. Instead, the horn  
561        focuses the proper sign parent  $\pi^\pm, K^\pm$  in such a configuration that the neutrino angle from  
562        the parent decay particles are focused in a beam.

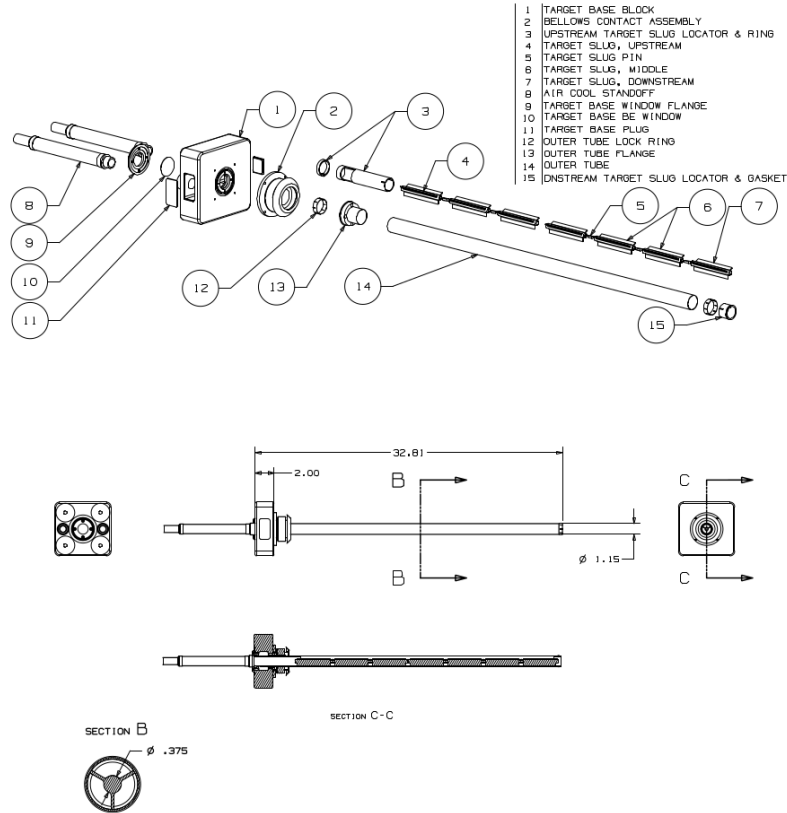


Figure 4.2: An exploded view of the BNB target which shows the 7 Beryllium slugs housed inside the support structure.

563 Directly downstream of the horn/target assembly is a collimator that is used to reduced  
 564 background coming from unwanted particles. Particles passing through the collimator enter  
 565 a 45 m long decay region. In this region, most of the particles decay to produced the neutrino  
 566 beam. At the end of the decay region there is a beam stop made of steel and concrete. There  
 567 is also an array of gas proportional counters to detect high energy muons that punch through  
 568 the beam stop. A diagram of the entire BNB system is shown in figure 4.3. When the horn  
 569 polarity focuses (negative) positive charged mesons a (anti)neutrino beam is produced.

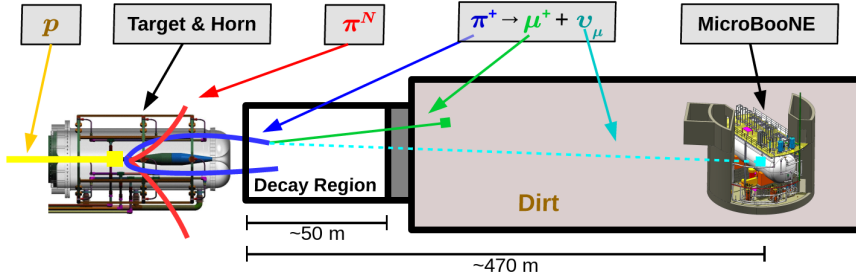


Figure 4.3: This figure shows the Booster Neutrino Beam line at FNAL. The neutrinos are produced in the decay region and then travel towards the MicroBooNE detector located 470 m down stream.

## 570 4.2 Neutrino Flux Prediction

571 The neutrino flux prediction for MicroBooNE uses the same GENIE simulation files used  
 572 by MiniBooNE.[14] The files are feed into a Geant4 module that simulates the particles  
 573 as they travel through the target, horn, and decay region. This produces a Monte Carlo  
 574 (MC) flux estimate for each of the various neutrino types.[15] A systematics study was then  
 575 performed to provide an error estimate for each of the  $\nu_e$ ,  $\bar{\nu}_e$ ,  $\nu_\mu$ , and  $\bar{\nu}_\mu$  flux predictions.  
 576 To do this, 6 primary systematics were varied: the production rates of  $\pi^+$ ,  $\pi^-$ ,  $K^+$ ,  $K^-$ ,  
 577 and  $K_L^0$ , and a group systematic comprised of the horn current miscalibration, skin depth,  
 578 nucleon inelastic, nucleon quasielastic(QE), nucleon total cross sections, pion inelastic, pion  
 579 QE, and pion total cross sections. Beam errors for each of systematics are shown in Table  
 580 4.1 .The final flux estimate with the error uncertainty is shown in Figure 4.4.

	$\nu_\mu$	$\bar{\nu}_\mu$	$\nu_e$	$\bar{\nu}_e$
Delivered P.O.T.	2.00%	2.00%	2.00%	2.00%
$\pi^+$	5.8%	0.46%	4.62%	2.66%
$\pi^-$	0.01%	7.51%	0.28%	3.20%
$K^+$	0.38%	0.13%	5.19%	2.61%
$K^-$	0.01%	0.35%	0.28%	3.92%
$K_l^0$	0.03%	0.27%	2.36%	22.59%
Other	5.78%	6.09%	3.6%	7.61%

Table 4.1: Systematic errors for production of various neutrino types with respect to their, P.O.T. , parent particle, and other variables.

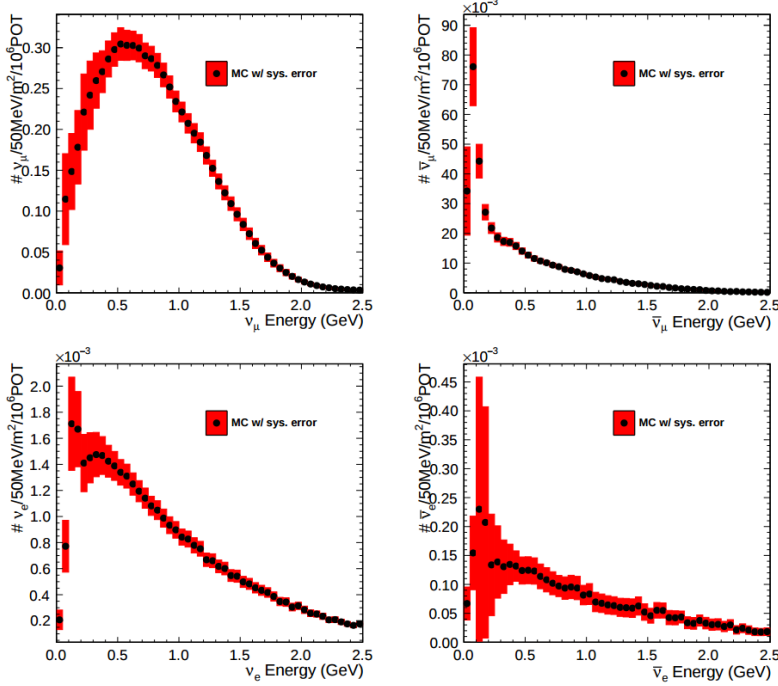


Figure 4.4: Monte Carlo flux predictions for the BNB neutrino spectrum. The red band represents the flux systematic errors. Note the orders of magnitude with the  $\nu_\mu$  spectrum rates.

## 581 Chapter 5

# 582 Low Energy Excess and Relevant 583 Cross Sections

### 584 5.1 Overview

585 This chapter will discuss various facets of what is commonly called the “MiniBooNE Low  
 586 Energy Excess.” First, we will present the anti-neutrino excess observed by LSND and how  
 587 the oscillation results can be interpreted. Then, we will discuss the efforts of MiniBooNE to  
 588 understand the LSND results along with their oscillation results that establish the “Mini-  
 589 BooNE Low Energy Excess.” We will also discuss the neutral current  $1\pi^0$  cross section  
 590 which is the dominant background in the oscillation analysis claims for both MiniBooNE  
 591 and LSND. Finally, we will discuss MicroBooNE’s role towards addressing understanding  
 592 the low energy excess claims of MiniBooNE.

### 593 5.2 LSND Excess

594 The Liquid Scintillator Neutrino Detector (LSND) was a 167 ton neutrino detector stationed  
 595 at Los Alamos National Lab (LANL) designed to study neutrino oscillations. The detector,  
 596 which hosted 1220 PMT’s for event detection, was placed 30 m away from the source of a  
 597 low energy ( 40 MeV)  $\bar{\nu}_\mu$  beam. Using the Los Alamos LAMPF beam, 800 MeV protons  
 598 interacted with a water target to produce  $\pi^+$  mesons which decayed into  $\mu^+ + \nu_\mu$ . The  $\mu^+$

599 would then interact with a copper beam stop and decay at rest to produce the low energy  
 600  $\bar{\nu}_\mu$  beam.

601 The detector medium was primarily carbon (mineral oil  $CH_2$ ). LSND could easily  
 602 distinguish between electromagnetic showers (electrons/positrons/photon) or tracks (pi-  
 603 ons/muons/protons) by differences in the Cherenkov cone that were produced. The oscil-  
 604 lation signal interaction was  $p + \bar{\nu}_e \rightarrow n + e^+$ . The primary  $e^+$  is easily visible from the  
 605 Cherenkov light it produced but a neutron would not have produced Cherenkov light and  
 606 therefore be invisible to the detector. The organic scintillator b-PDB was dissolved in the  
 607 mineral oil at a concentration of 31 mg/l. The scintillator allowed the 2.2 MeV photon from  
 608 the capture of the neutron on hydrogen to be detected. This allowed LSND a unique signal  
 609 to identify  $\bar{\nu}_e$  interactions. It should be noted that the detector technology could not easily  
 610 discriminate between photons, electrons or positrons induced electromagnetic showers.

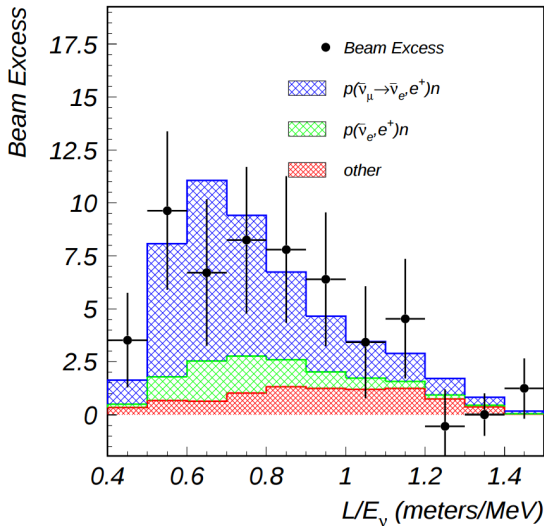


Figure 5.1: This is the LSND neutrino oscillation appearance plot as a function of  $L/E$  and represents the 87 event  $\bar{\nu}_e$  excess claimed by the experiment.

611 In 2001, the collaboration published results for an observed excess of  $87 \pm 22.4$  statistical  
 612 , $\pm 6.0$  *systm* events above the predicted background as shown in figure 5.1. If the excess is  
 613 interpreted as neutrino oscillations from a two neutrino model, the best fit of the excess  
 614 would suggest a  $\sin^2(2\theta) = 0.003$  and  $\Delta m^2 = 1.2\text{eV}^2$  which greatly contradicts many other  
 615 measurements for  $\Delta m_{2,3}^2$  or  $\Delta m_{1,3}^2$  [16]. One explanation for the excess suggests the idea of  
 616 mixing between other additional neutrino states. These neutrinos are called ‘sterile’ since  
 617 they cannot directly couple via weak interaction as mentioned prior from the constraints  
 618 from LEP.

### 619 5.3 MiniBooNE Excess

620 The Mini Booster Neutrino Experiment (MiniBooNE) was designed to address the claims of  
 621 the LSND  $\bar{\nu}_e$  excess result. The MiniBooNE detector was a mineral oil Cherenkov detector  
 622 designed to be a similar technology to LSND[17]. MiniBooNE, stationed at FNAL in the  
 623 BNB, was positioned 541 m from the neutrino source and was able to receive both  $\nu_\mu$  and  
 624  $\bar{\nu}_\mu$  fluxes. The distance was chosen such that the  $L/E$  parameter were similar to that of  
 625 the LSND experiment.

626 MiniBooNE, which contained 818 tons of mineral oil ( $CH_4$ ), was located underneath  
 627 more than 3m of earth overburden to help reduce cosmic rays. The detector supported a 35  
 628 cm thick outer cosmic veto using 240 PMT’s. The veto efficiency was 99.99% for rejecting  
 629 cosmic muons. The inside of the detector was instrumented with 1,280 8-inch PMT’s  
 630 which were used to read out neutrino and comsic data. Cherenkov light from different  
 631 particles produced distinct patterns on various PMT’s inside the spherical detector. A  
 632 cartoon showing various type of signal topologies from the MiniBooNE detector is shown  
 633 in figure 5.2. The detector energy scale was calibrated *in situ* by fitting various parameters  
 634 from through going muons, decay Michele electrons, and  $\pi^0$  decay’s. A clear limitation of  
 635 Cherenkov detectors is the inability to concretely distinguish between photon induced or  
 636 electron induced showers.

637 The primary oscillation analysis for MiniBooNE was done ‘blind’ in an attempt to  
 638 gain confidence from the physics community upon its findings[18]. The entire analysis was

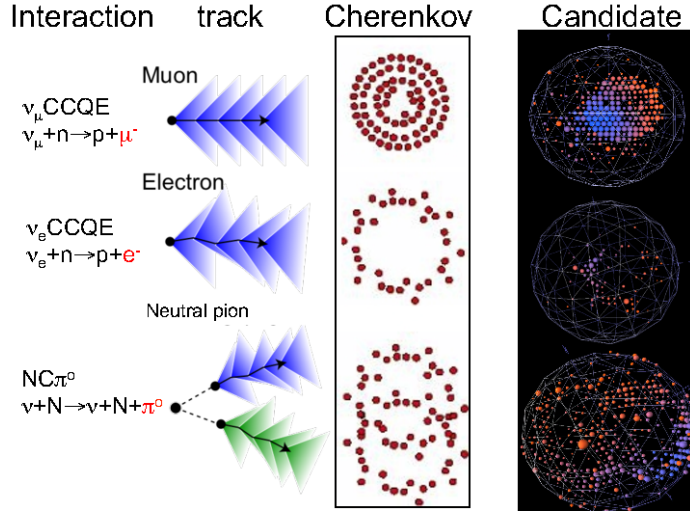


Figure 5.2: This cartoon depicts different particle interactions as observed in Cherenkov detector. The far right shows the interaction types as viewed in MiniBooNE

639 developed on large statistics Monte Carlo simulation and a small sample of test data. In  
 640 total, MiniBooNE accumulated  $6.46 \times 10^{20}$  P.O.T. of  $\nu$ -data and  $11.27 \times 10^{20}$  P.O.T. of  
 641  $\bar{\nu}$ -data. Fermilab's ability to support both neutrino and anti-neutrino beams allow for  
 642 MiniBooNE to confirm that an LSND-like excess was independent of neutrino type. The  
 643 data is in good agreement between signal and background predictions and contradicts the  
 644 LSND claim up to 98% confidence in both modes above 500 MeV. The excess is most  
 645 prominent in the region of events below 500 MeV, as seen in figure 5.3. In this region  
 646 the largest background comes from  $\pi^0$ -misidentification followed by photons coming from  
 647 radiative  $\Delta$  decays. MiniBooNE reports a total excess of  $240.0 \pm 62.9$  combined,  $(162.0 \pm$   
 648  $47.8\nu, 78.4 \pm 28.5\bar{\nu})$  events in the neutrino energy range  $200 < E_\nu^{QE} < 1250\text{MeV}$ . Also,  
 649 if the excess is interpreted as a two flavor oscillation the inferred parameters are consistent  
 650 with the LSND result.

## 651 5.4 Neutral Current $\pi^0$ production

652 The leading background from the MiniBooNE oscillation result, as mentioned in chapter 5.3,  
 653 is  $\pi^0$ -misidentification. Accurately measuring the neutrino induced neutral current single

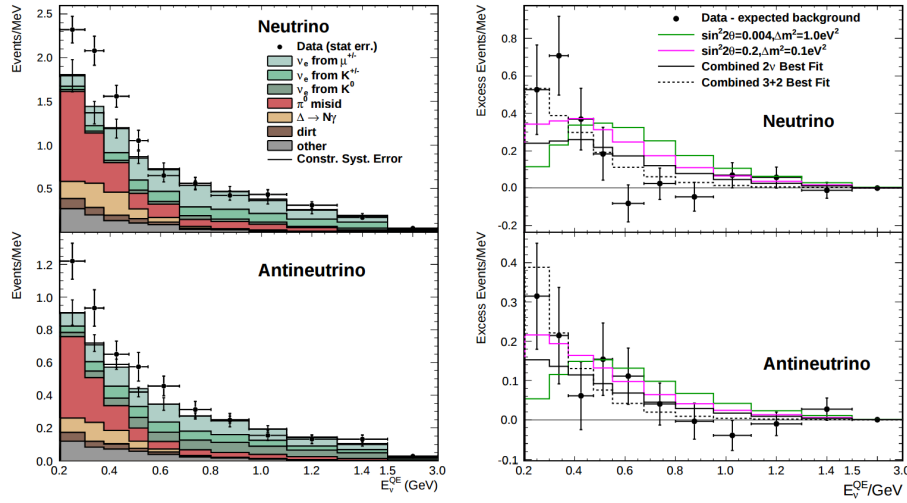


Figure 5.3: The left plots show the stacked histograms for signal and background overlaid with data for both neutrino and anti-neutrino modes. The right plots show the relative excess as a function of neutrino energy and make obvious the energy range that drives the excess.

$\pi^0$  production cross section is therefore crucial in understanding background contributions for an oscillation analysis. Charge current  $\pi^0$  production conveniently has an outgoing charged muon in the final state and is very easy to identify. On the other hand, neutral current  $\pi^0$  production does not guarantee any outgoing charged particles and therefore, makes identification much harder. For neutrinos in the BNB, the main production mode for neutrino induced neutral current  $\pi^0$  production is via the  $\Delta(1232)$  resonant production. Resonant production is when a baryon, such as a proton or neutron, is excited to a higher resonance state and then subsequently decays back to the initial state while liberating a  $\pi^0$ . There are other neutrino induced  $\pi^0$  production modes that MicroBooNE is sensitive to such as deep inelastic scattering and coherent production, but have a lower production cross section at the given BNB neutrino energy range. A general Feynman diagram can be used to describe the main components of neutrino induced neutral current single  $\pi^0$  production in argon as seen in Figure 5.4.

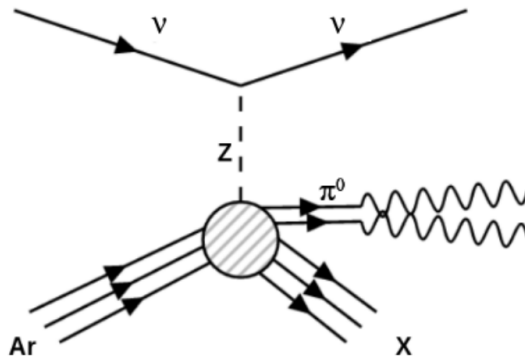


Figure 5.4: Neutrino induced single  $\pi^0$  production on argon. This topology is defined such that single  $\pi^0$  is produced and the other particles leaving the interaction ( $X$ ) must only consist of nucleons.

## 667 5.5 NC- $\pi^0$ in Carbon vs Argon

668 In 2010, MiniBooNE measured the total neutral current single  $\pi^0$  cross section on carbon  
 669 with what is currently the world's largest statistics sample of  $\pi^0$ s. The MiniBooNE neutral  
 670 current single  $\pi^0$  signal is defined as a topology that produces one and only 1  $\pi^0$  in the  
 671 final state with no other other charged leptons or mesons originating from the vertex. In  
 672 2015, the first measurement of neutrino induced neutral current  $\pi^0$  production on argon was  
 673 measured by ArgoNeut collaboration at Fermilab while running in the NuMI neutrino beam.  
 674 AgroNeut, being a smaller detector, could not easily contain many of the electromagnetic  
 675 showers from  $\pi^0$  decays. This forced the analysis choose a slightly different final state signal  
 676 definition requiring there to be at least one  $\pi^0$ , no electron or muon, and allowing there  
 677 to be any number of mesons in the final state. This modified signal definition makes any  
 678 comparison to other historical data very complicated.

679 MicroBooNE, which resides in the same neutrino beam line as MiniBooNE, is a prime  
 680 candidate for various studies of neutral current  $\pi^0$  production studies between different  
 681 target materials (C/Ar). Being a larger LArTPC, more  $\pi^0$  decays will be contained allowing  
 682 for high statistics measurements of the cross section along with the general need to measure  
 683 the production rate as input to its own oscillation analysis.

## 684 Chapter 6

# 685 Cosmogenic $\pi^0$ s at MicroBooNE

686 In this chapter we will talk about some of the challenges and interesting physics cases re-  
687 garding cosmogenics in a surface LArTPC. Many cosmic ray particles penetrate surface  
688 detectors and populate the detector region making it necessary to remove these particles  
689 from reconstruction and address charge contamination in neutrino events. The majority  
690 of this chapter will emphasize cosmogenic track removal, electromagnetic showers and sub-  
691 sequently  $\pi^0$  selection. We will first examine some historical cosmogenic studies from the  
692 Icarus experiment. Then, introduce what MicroBooNE can contribute in terms of un-  
693 derstanding cosmics. We will address the cosmic simulation that is used, various steps in  
694 reconstruction and pattern recognition used to select  $\pi^0$ s in a LArTPC. Finally, we will con-  
695 clude with how these studies impact future cross section analyses and backgrounds toward  
696 the low energy excess analysis.

### 697 6.1 Motivation

698 Cosmogenic particles allow for the separate test of reconstruction tools along with an inde-  
699 pendent way to address the detector energy scale. The high rate of surface cosmics cause  
700 some trouble with disentangling signal neutrino events from cosmic ray removal. Luckily, off  
701 beam surface cosmogenic samples allow for a large statistics dataset to develop and optimize  
702 reconstruction techniques. Cosmogenic muons that traverse the detector provide a handle to  
703 understand detector energy scale along with understanding track reconstruction efficiency.

704 Stopping muons that produce a Michele electron help provide a benchmark for low energy  
 705 showers in the 10's of MeV range. The  $\pi^0$  resonance, with a mass of  $134.9 \text{ MeV}/c^2$ , can  
 706 be used as a standard candle to benchmark overall detector energy scale. The calculated  
 707 the  $\pi^0$  mass, as shown in equation 6.1, depends on a measurement of energy and photon  
 708 opening angle.

$$\mathcal{M} = \sqrt{2E_1E_2(1 - \cos\theta_{12})} \quad (6.1)$$

709 Electromagnetic shower reconstruction for LArTPC's is well known to be a hard task.  
 710 The high resolution of the 2-dimensional projections of EM-showers introduce many chal-  
 711 lenges to develop unbiased and fully automated reconstruction. In 2001, the T600 ICARUS  
 712 detector ?? performed a surface test run in Pavia, Italy. During this 100 day test the detec-  
 713 tor collected over 30,000 cosmic ray events. In 2008, the ICARUS collaboration published  
 714 a study of electromagnetic showers coming from  $\pi^0$  decays in the Pavia dataset. To select  
 715 candidate  $\pi^0$  events, ICARUS hand scanned a total of 7,500 potential events from a PMT  
 716 triggered sample. Their hand scanning requirements included, that at least two well sep-  
 717 arated electromagnetic showers were visible, a valid  $t_0$  time for the vertex, and that there  
 718 was not much charge contamination coming from a nearby cosmic muon. After this, they  
 719 were left with 212 hadronic interactions with at least one candidate neutral which they then  
 720 proceeded to reconstruct. Their final reconstruction consisted of energy scaling to account  
 721 for missing charge in the shower and a minimization against the true  $\pi^0$  mass. An example  
 722 of one of their hand scanned clustering events is shown in Figure 6.1.

723 MicroBooNE, being a surface detector, is in a position to do a similar study with im-  
 724 proved reconstruction techniques. Also, understanding the cosmic production rate for single  
 725  $\pi^0$ s is valuable to any MicroBooNE analysis that involves EM-showers. The following sec-  
 726 tions will present MicroBooNE's Monte Carlo simulation and state of the art reconstruc-  
 727 tion techniques.

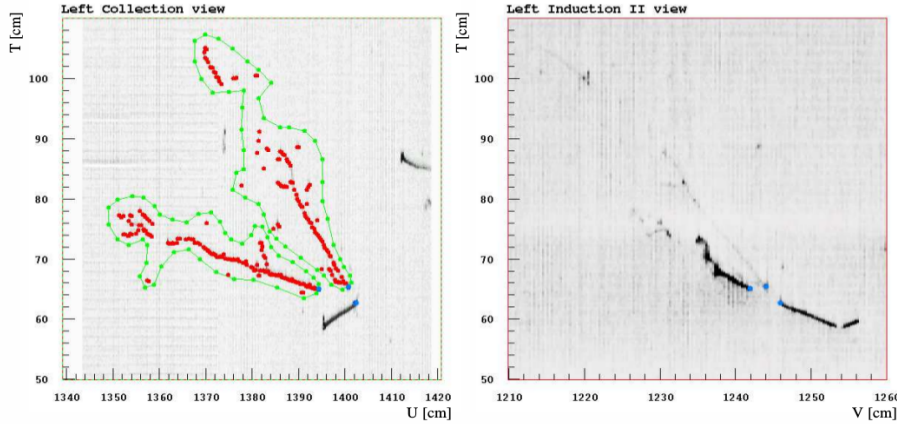


Figure 6.1: A cosmic  $\pi^0$  from the ICARUS Pavia run. The left image shows the hand drawn clustering and positions of the shower conversion point and vertex point. The right image shows the same event on a different wire plane view.

## 6.2 Traditional Reconstruction

The traditional approach for LArTPC reconstruction involves grouping drift charges that are deposited on the wires to form wire-hits. The light collection system also has light-hits which corresponded to collected light of an individual track or shower. A group of PMT's that have light-hits at the same time is called a flash. Hits from each of the wire planes are clustered together with various reconstruction algorithms to form reconstruction objects that relate to individual particles in the detector. There are two primary reconstruction objects: tracks, which are mostly linear and compact clusters that represent muons, protons, and charged pions, and showers which are more fuzzy shaped cluster objects that represent photons and electrons. Next, to reconstruct a 3D object, an algorithm must match the same 2D cluster objects in at least two of the three wire planes. For MicroBooNE, and the general LArTPC community, matching track reconstruction is well advance but shower reconstruction suffers many pitfalls. In recent years lots of progress has been made for LArTPC shower reconstruction. Various different techniques such as improved 2D clustering and matching techniques, sophisticated pattern recognition tools[19], and deep learning[20] approaches have been explored and each has its various strengths and weaknesses.

### 744 6.3 Wire Cell Imaging

745 The traditional approach is not the only way to reconstruct LArTPC data. Instead, wire  
 746 data can be treated with a tomographic approach directly producing a set of 3D space  
 747 points. Although computationally intensive, this approach allows for more information to  
 748 be used in a 3D clustering framework which can directly impact shower reconstruction and  
 749 mitigate degeneracies from the 2D matching method.

750 The Wire-Cell framework, spearheaded by Brookhaven National Labs (BNL), utilizes  
 751 this approach to create 3D space points from MicroBooNE's TPC data. The approach  
 752 relies on the assumption that the same amount of ionization charge is seen on each plane.  
 753 In MicroBooNE this is done by reconstructing small time slices on each wire planes. Each  
 754 time slice involves solving a charge equation for all possible hits with respect to the matrix of  
 755 hits actually recorded in the time slice. The charge equation is shown in equation 6.2. The  
 756 detector wire signals are represented in matrix W while all potential wire hits are contained  
 757 in H. Nonzero values in the Q matrix will correspond to unique wire-plane intersections of  
 758 charge, near zero values represent ghost hits due to degeneracies in the charge equation.

$$\begin{bmatrix} W_{u_1} \\ \vdots \\ W_{u_n} \\ W_{v_1} \\ \vdots \\ W_{v_n} \\ W_{y_1} \\ \vdots \\ W_{y_n} \end{bmatrix} = \begin{bmatrix} Q_{u_1}^{H_1} & Q_{u_1}^{H_2} & \dots & \dots & \dots & Q_{u_1}^{H_{m-1}} & Q_{u_1}^{H_m} \\ \vdots & \vdots & \ddots & \ddots & \ddots & \vdots & \vdots \\ Q_{u_n}^{H_1} & Q_{u_n}^{H_2} & \dots & \dots & \dots & Q_{u_n}^{H_{m-1}} & Q_{u_n}^{H_m} \\ Q_{v_1}^{H_1} & Q_{v_1}^{H_2} & \dots & \dots & \dots & Q_{v_1}^{H_{m-1}} & Q_{v_1}^{H_m} \\ \vdots & \vdots & \ddots & \ddots & \ddots & \vdots & \vdots \\ Q_{v_n}^{H_1} & Q_{v_n}^{H_2} & \dots & \dots & \dots & Q_{v_n}^{H_{m-1}} & Q_{v_n}^{H_m} \\ Q_{y_1}^{H_1} & Q_{y_1}^{H_2} & \dots & \dots & \dots & Q_{y_1}^{H_{m-1}} & Q_{y_1}^{H_m} \\ \vdots & \vdots & \ddots & \ddots & \ddots & \vdots & \vdots \\ Q_{y_n}^{H_1} & Q_{y_n}^{H_2} & \dots & \dots & \dots & Q_{y_n}^{H_{m-1}} & Q_{y_n}^{H_m} \end{bmatrix} \begin{bmatrix} H_1 \\ H_2 \\ \vdots \\ H_{m-1} \\ H_m \end{bmatrix} \quad (6.2)$$

759        Then, each ‘slice’ is stacked to it’s corresponding x position. This produces a set of 3D  
760        space points that can used in patter recognition algorithms to identify different particles  
761        in the data. All reconstruction is done with accounting for known detector dead regions.  
762        The current state of MicroBooNE’s signal and noise processing and imaging that requires  
763        a minimum of 2 wire planes to be matched from the charge equation.

## 764        6.4 Pattern Recognition

765        Various pattern recognition tools are needed to address MircoBooNE’s TPC data but for  
766        this analysis they can be generalized into two efforts, cosmic track removal and EM-shower  
767        clustering. Both approaches require different techniques. First, we will focus on optimizing  
768        track removal. This involves identifying tracks that are through-going, and contained. Once  
769        all the charge associated with tracks are removed, the remaining charge is clustering into  
770        candidate EM-shower objects. Finally, correlated shower pairs are identified and selected  
771        as candidate  $\pi^0$ events.

772        A image of a typical MicroBooNE cosmic event reconstructed with 3D wire cell space  
773        points are shown in Figure 6.2 using the BEE viewer [21]. A detailed list of reconstruction  
774        and selection parameters are listed in the appendix.

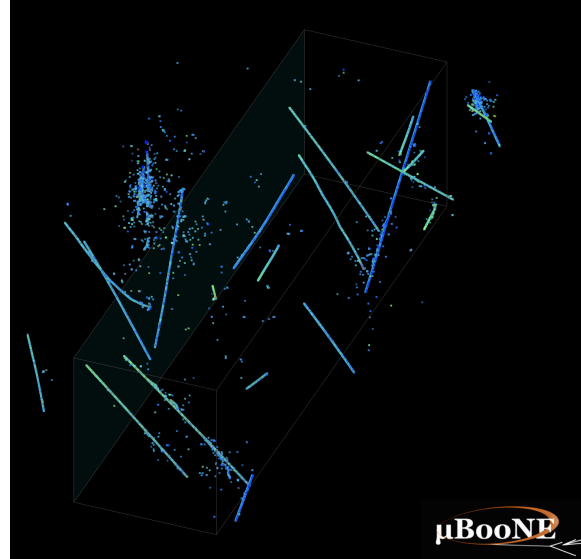
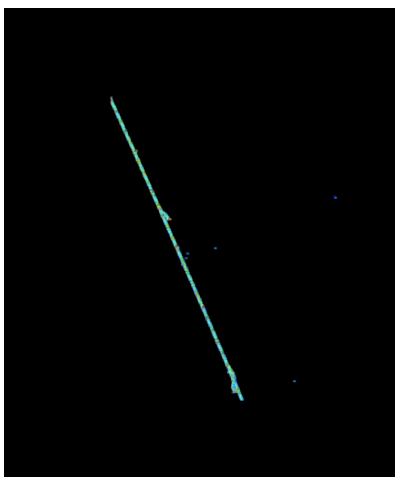


Figure 6.2: This is a typical cosmic event in the MicroBooNE detector. The data used to generate this event is CORSIKA Monte Carlo.

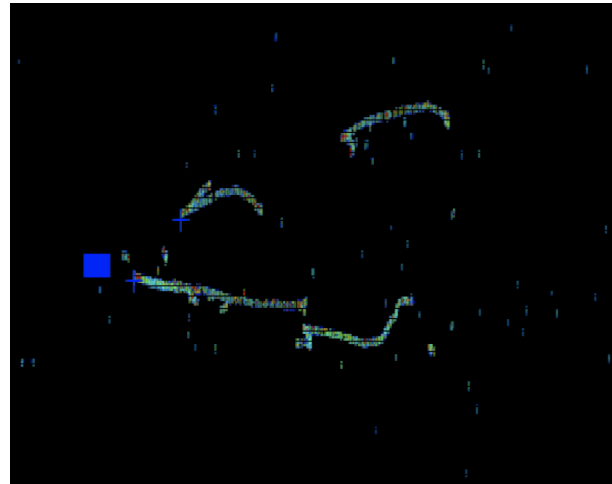
## 775 6.5 Clustering

776 The wire cell data produces a set of 3D space points as mentioned in section 6.3. Only space  
 777 points that are in the fiducial volume are clustered and considered in the reconstruction  
 778 process. First a charge threshold cut of 0.5 MeV is applied to all the remaining space points.  
 779 This is to remove very low charge ghost points and reduce the overall number of points to  
 780 cluster. The main goal of this step is to identify the large scale structure of the cosmic  
 781 tracks in the data. Additionally, with a smaller number of space points the computational  
 782 time for reconstruction is reduced.

783 The first stage of clustering uses BIRCH (balanced iterative reducing and clustering  
 784 using hierarchies). The hyper parameters were tuned such that cosmic tracks are removed  
 785 with minimal impact to showers involved from  $\pi^0$ . Birch clustering was chosen because it  
 786 scales well with large number of points, efficiently maintains large number of clusters in  
 787 datasets and also handles outliers removal well. This clustering technique leverages on the  
 788 inherent structure of charged particle tracks having a well define 3-dimensional trajectory.  
 789 Particles such as protons, muons, and charged pions are continuously ionizing meaning  
 790 that there should be not be gaps in the detected charge. This feature is much different than



(a) This figure shows an image of muon track as viewed from the BEE-WireCell image viewer.



(b) This figure shows an image of  $\pi^0 \rightarrow \gamma\gamma$  decay as viewed from the BEE-WireCell image viewer.

791 EM-showers which have lots of gaps between detected charge. An example of this is shown  
792 in figure 6.5

793 The next stage of the track and shower clustering process is to merge together proto-  
794 clusters that did not get fully grouped together in the BIRCH clustering step. The second  
795 pass clustering is geared toward larger object clustering. To address this, a 3D convex hull  
796 is constructed around every cluster. Next, the euclidean distance between all the vertex  
797 points are calculated. If the minimum merging distance is small, as it is for many charge  
798 particle tracks, the clusters get merged together well. Clusters from showers, as they tend  
799 to be very spread out, still need further merging.

800 The final stage of clustering is shower clustering. This requires there to be a distinction  
801 between a cluster object that is shower-like or track-like. To do this, parameters that  
802 describe various aspects of a cluster are calculated. The most important features from the  
803 cluster parameters are cluster length and spread of the first principle component. More  
804 details about track and shower selection are described later in section 6.6.

805 Once defined as a proto-shower cluster, a 3D charge weighted axis is fit to the cluster's  
806 set of space points. The next step is to merge together proto-showers into their respective  
807 showers. The goal for this step is to merge together proto-showers that originate from a

808 primary shower. To do this, a distance of closest approach (DOCA) for each proto-shower  
 809 cluster axis pair is calculated along with the midpoint from the DOCA line for each pair.  
 810 Next, a the closest distance from the midpoint to both showers are calculated. The angle  
 811 between the two proto-shower axis is also calculated. A pair of proto-showers that have  
 812 a DOCA that is less than 5 cm, an angle between 15 and 165 degrees, and both of the  
 813 conversion lengths are less than 20 cm are merged together. The merging is done for all  
 814 proto-shower cluster pairs as a final stage of the merging process.

## 815 6.6 Track and Shower Selection

### 816 6.6.1 Track Removal

817 For this analysis track removal is handled in a unique manner. The primary goal is to  
 818 identify showers coming from a  $\pi^0$ . Therefore, all cuts and optimizations will be tested  
 819 against shower objects. Being that we simply are trying to identify charged tracks and not  
 820 particle type, the charge information is not used. The general approach for track removal  
 821 depends heavily on geometric properties such as length and linearity of the cluster.

### 822 6.6.2 Single $\pi^0$ Reconstruction

823 The vast majority (98.8%) of  $\pi^0$ s decay into two photons. The relationship for the particle  
 824 mass, which was defined in eq 6.1, shows the importance of properly accounting for the  
 825 energy and angle between the decay photons. To understand a baseline for reconstruc-  
 826 tion efficiency we have generated a sample of 10,000 single particle  $\pi^0$  events isotropically  
 827 throughout the detector volume with initial momenta spanning from 0 to 2 GeV.

828 First we will investigate energy deposited in detector from the decay. An plot of the true  
 829 kinematic energy of photons from the decay particle is shown in Figure 6.3. It is important  
 830 to note that both photons need to be reconstructed to form a mass. This means that we  
 831 are driven to optimize the reconstruction to be robust around showers in the range of many  
 832 tens of MeV in deposited energy. Photons that convert near the fiducial edge of the detector  
 833 can escape and deposit only a small amount of energy in the detector. This poses problems  
 834 for capturing the total amount of energy of the shower and drives the need for a fiducial

835 cut around the edges.

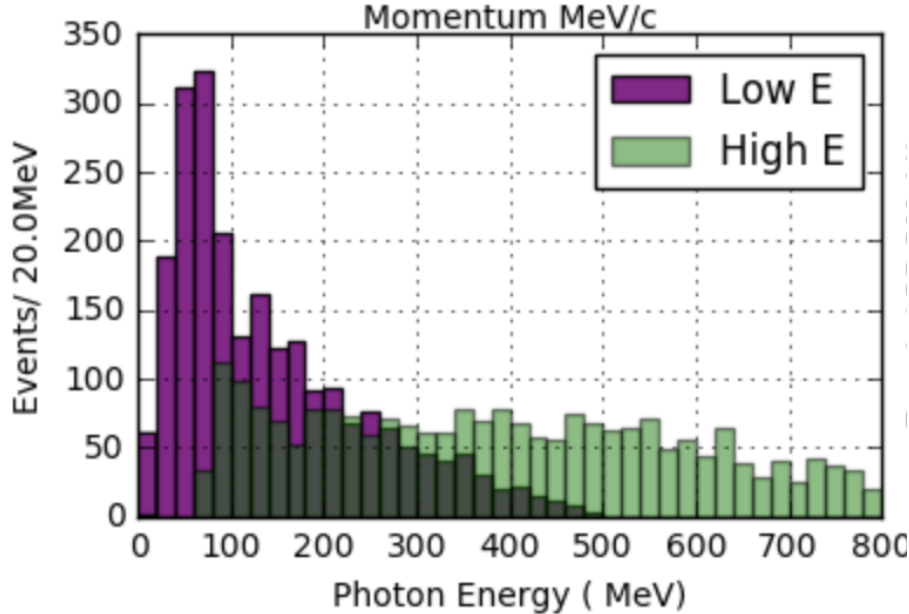
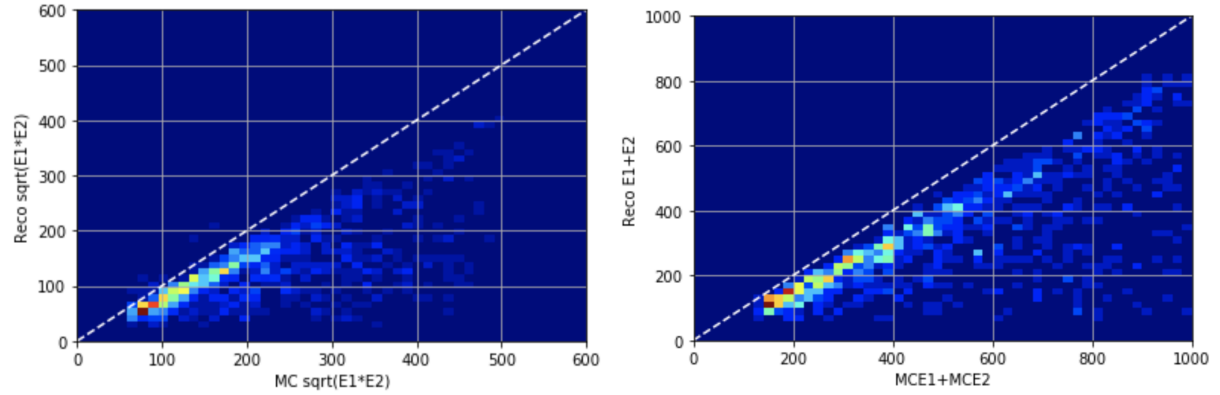


Figure 6.3: This figure shows the photon distribution for  $\pi^0$  decays from a single particle sample of between 0-2 GeV. The higher energy photon is shown above in green along with the corresponding lower energy photon shown in magenta.

836 To understand the reconstruction accuracy for the energy we are most interested in two  
 837 metrics. The first is the total collected energy deposited by the two showers. This informs  
 838 us that we are accounting for most of the energy deposited and handling the fiducial cuts  
 839 well. The second is the product of the two shower energies. This directly impacts the  
 840 reconstructed mass resolution and informs us that we are clustering energy between the  
 841 two showers properly. In figure 6.4 both metrics are plotted for reconstruction against true.  
 842 Points along the diagonal would represent accurate model predictions. As we will see later  
 843 in this chapter, the energy product drives the width of the mass resolution.

844 Next we will investigate the effects of the opening angle between the two photons.  
 845 The minimum opening angle of the photons is constrained by the momentum boost as  
 846 the particle decays as shown in equation 6.3. The angular resolution is a very challenging  
 847 problem in LArTPC's using the traditional 2D projection approach. Fortunately, direct



(a) Scatter plot of reconstructed energy product vs true energy sum  
(b) Scatter plot of reconstructed energy sum vs true energy product

Figure 6.4: Reconstructed energy sum and energy product for shower pairs. Both, the reconstructed energy sum and product is less than the true energy deposited.

848 3D reconstruction improves the angular resolution and allows for a better measurement of  
849 shower direction.

$$\sin \frac{1}{2} \theta_{min} = \frac{M}{E_{\pi^0}} \quad (6.3)$$

850 A plot of the reconstructed vs true opening angle is shown in Figure 6.5. The  $1 - \cos\theta$   
851 term from equation 6.1 is sensitive to tails of the mass distribution.

852 Next, we apply a final set of selection cuts. First, we require that the distance of  
853 closest approach between the two shower axis is less than 5 cm. This is to help ensure  
854 that the photons are originating from a common origin. Next, we calculate the opening  
855 angle between the two showers and require the angle to be within the range of 20 deg -  
856 160 deg. Also, the photon conversion distance can not be longer than 70 cm for each of  
857 the showers. This is done to help identify showers that are correlated from the same decay.  
858 Finally we only accept showers that are above 50 MeV in reconstructed energy. Figure 6.6  
859 shows the effect of various parameters as applied to the reconstruction. We find that the  
860 deficit in mass peak is mainly due to the energy reconstruction. This is due to the missing  
861 energy during clustering. For this analysis there is also an additional component of energy

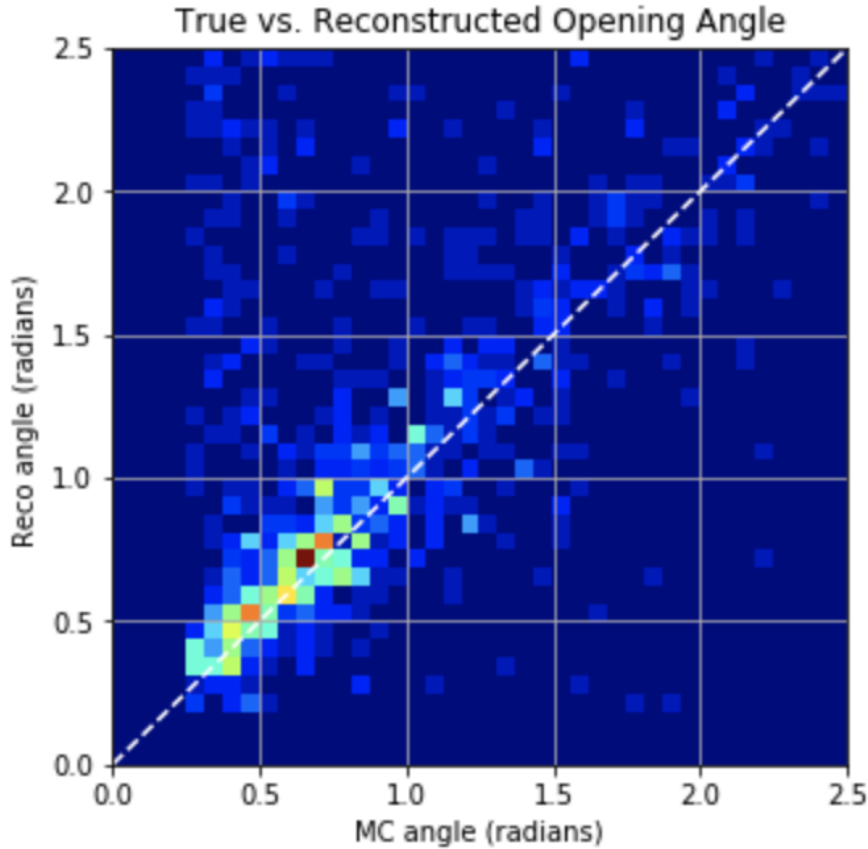


Figure 6.5: This scatter plot shows the reconstructed opening angle vs. true opening angle. We see that the reconstruction does very well with reconstructing this quantity due to the use of wire-cell's 3D approach. When the reconstruction performs badly it tends to identify small opening angles as large ones since we are not using any vertex information.

missing since we will not be using the initial  $t_0$ -tag. The  $t_0$ -tag is used to identify how far the electrons had to drift to reach the wire plane. Without using  $t_0$ , there is no effective way to correct back for electron drift effects. Thankfully, this effect is can be captured in understanding the distribution of reconstructed mass peak in the Monte Carlo.

Finally, we address the over all efficiency for reconstruction. The average reconstruction efficiency between 0 and 1 GeV/c is 40.1%. The reconstruction efficiency is shown in Figure 6.7. As can be seen there, the efficiency drops at low and high energies. At low momentum the  $\pi^0$ s are produced nearly at rest with both showers having similar energies.

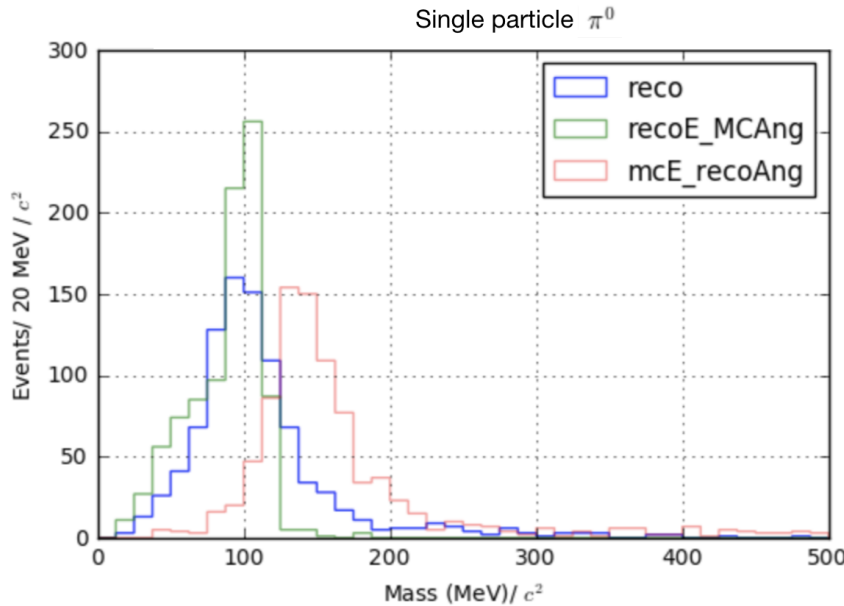


Figure 6.6: The reconstructed mass distribution is shown to highlight effects from reconstruction. First, in blue, the full reconstructed mass is shown. Second, in green, the reconstructed mass is calculated using the true angle. Third, in red, the reconstructed mass is calculated using the true energy.

870 Most importantly the showers are produced nearly back to back. Without having a well  
 871 defined vertex, sometime the reconstruction will identify the angle as being close to zero.  
 872 Being that there is a minimum opening angle cut some of the events are lost from this effect.  
 873 At high momentum, many of the showers are boosted to small opening angle which we see  
 874 a similar effect in the loss of efficiency.

## 875 6.7 Single $\pi^0$ cosmic sample

876 The MicroBooNE cosmis Monte Carlo is generated by CORSIKA (COsmic Ray Simulation  
 877 for KAscade) v-7.4003[22]. CORSIKA simulates particles coming from a wide range of  
 878 interactions initiated by cosmic ray particles in the upper atmosphere. The simulation is  
 879 robust and accounts for various input parameters such as, longitude and latitude, elevation,  
 880 and the earths magnetic field. The particles are simulated over a large region above the

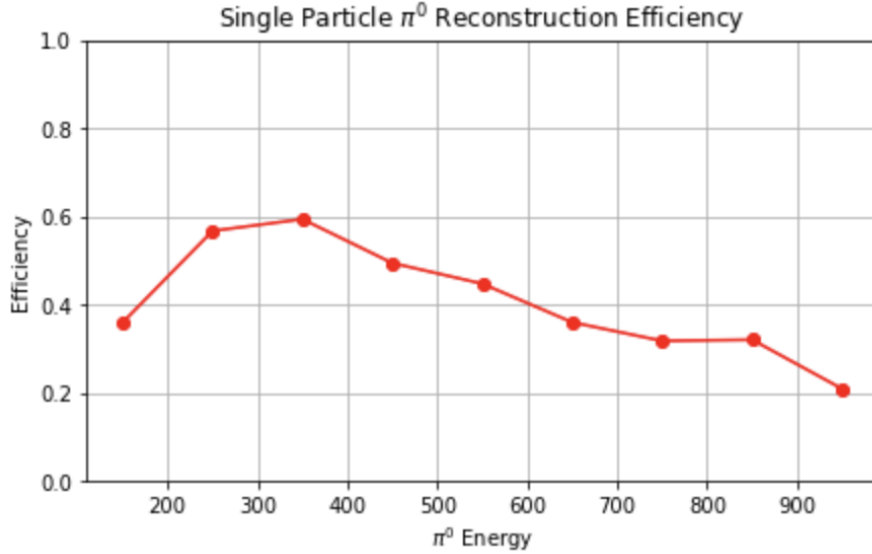


Figure 6.7: The plot shows the  $\pi^0$  reconstruction efficiency for  $\pi^0$ s over a 1,000-10,000 MeV energy range. The reconstruction efficiency peaks around 350 MeV which conveniently is around the production energy for cosmic  $\pi^0$

881 detector complex but only particles that travel through the detector cryostat volume are  
 882 kept. The passage of these particles is simulated by the GEANT4 package. Cosmic rays  
 883 that do not travel through the cryostat have a low likelihood of producing secondary or  
 884 tertiary particles that enter the detector TPC volume [23].

885 In one MicroBooNE drift window (2.3ms) there are on average 6 cosmic muons. The  
 886 muons do not directly contribute to many EM-showers but sometimes pass through an EM-  
 887 shower from another particle. For MicroBooNE, the vast majority of muons are through  
 888 going and do not lead directly to any method of  $\pi^0$  production.

889 Various other particles such as, protons, neutrons, and charged pions enter the TPC  
 890 volume and may produce  $\pi^0$ s. A distribution of  $\pi^0$  production process is shown in Figure  
 891 6.8. Nearly half of the  $\pi^0$ s produced in the MicroBooNE TPC are produced through neutron  
 892 inelastic scattering.

893 In total, 90,297 CORSIKA truth events were produced to constrain production rates for  
 894 signal and background. From that, a random sample of 10K events were ran through the  
 895 wire-cell imaging reconstruction. Additionally, a signal sample of events which contain a

896 single neutron  $\pi^0$  of  $\approx 1.2\text{K}$  was produced and reconstructed through the wire-cell imaging.  
 897 The exact rates will be discussed in Chapter 7.

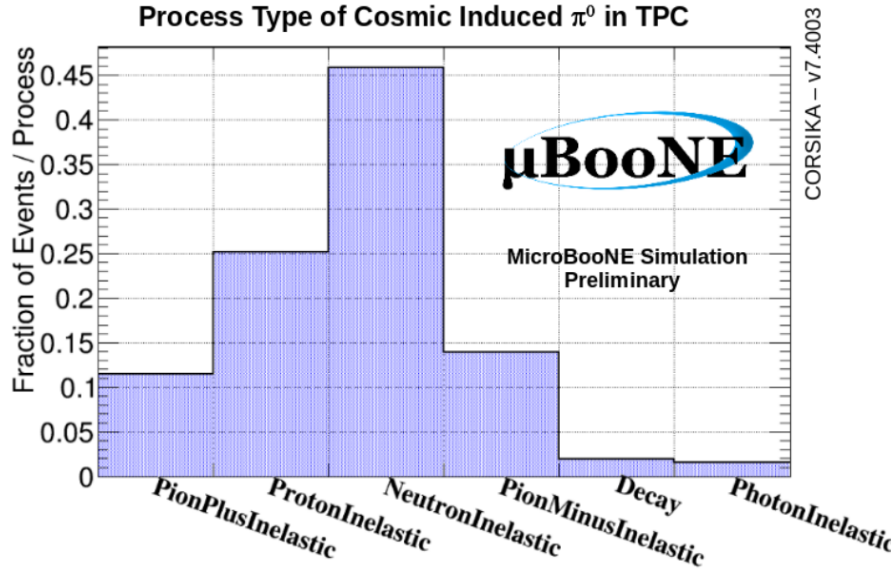


Figure 6.8: Physical process for cosmic  $\pi^0$  that decay inside the TPC.

898 MircoBooNE, being a surface detector, has very minimal shielding from cosmic rays.  
 899 Most of the  $\pi^0$ s coming from protons and charge pions do not make it very far into the  
 900 detector fiducial volume due to hadronic interactions outside the detector. The building  
 901 and cryostat easily absorb and re-scatter hadronic particles. This coupled with the argon  
 902 that is above the TPC provide reduction in charged hadronic particles that make it to the  
 903 fiducial volume. The neutrons do not interact as much and are slightly more distributed  
 904 over the TPC fiducial volume. A stacked scatter plot is shown in figure 6.9

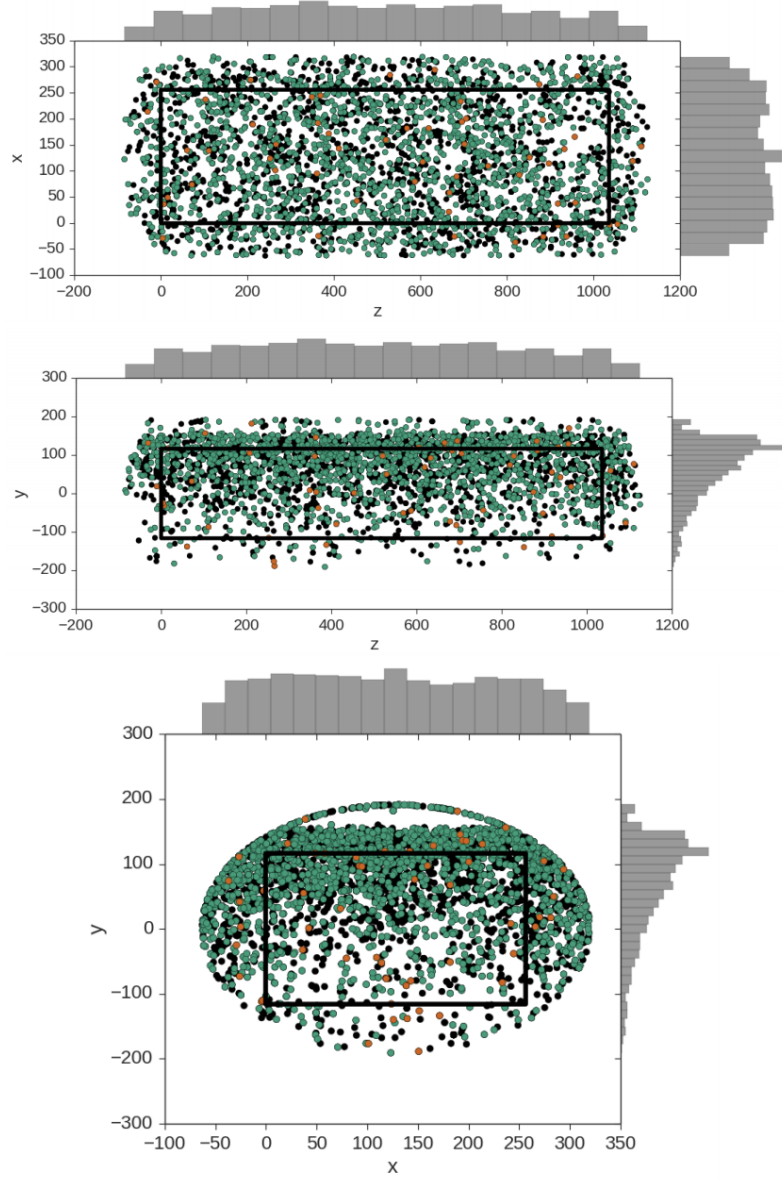


Figure 6.9: These plots show the decay point of actual cosmic  $\pi^0$ s throughout any time in the 4.8 ms window. The green points represent neutron induced  $\pi^0$ s, the orange represent photon induced  $\pi^0$ s, and the black represent a  $\pi^0$  that was produced from a charged particle. In each plot the black box is to represent the entire TPC dimensions not including fiducial cuts. Note that this is a stacked scatter plot with ordering; charged particle (black), photon (orange), neutron (green) from bottom to top.

# 905 Chapter 7

## 906 Results

907 The goal of this study is primarily two fold. The first goal is to highlight a different technique  
908 to reconstruct  $\pi^0$  and EM-showers in an LArTPC. To best showcase this reconstruction tech-  
909 nique we will focus on reconstructing  $\pi^0$ s that are induced from a single neutron. In many  
910 instances, neutral induced interactions do not have a visible vertex. Reconstructing EM  
911 showers from a  $\pi^0$  decay without a vertex poses many challenges for traditional techniques.  
912 The Wire-Cell imaging approach allows for a full 3D shower reconstruction without the use  
913 of a vertex. The second goal is to measure and compare the cosmic ray neutron induced  
914  $1-\pi^0$  production rate in the MicroBooNE detector. This reconstruction technique is well  
915 suited for this type of analysis.

916 This section will address results from both Monte Carlo and actual MicroBooNE cosmics  
917 data. To be clear, we will define our signal to be events that produce 1 and only 1 neutron  
918 induce single  $\pi^0$  inside the TPC fiducial volume. For this analysis the fiducial volume is  
919 defined from: X [0 cm, 256 cm] , Y[-116 cm, 116 cm], Z[400 cm, 800 cm]. We also restrict  
920 our bounds to events that happen in 1 drift window as defined in section 6.7 .

### 921 7.1 Monte Carlo Simulation

922 First, a word on simulation constraints. While the wire-cell imaging process provides con-  
923 siderable gains towards extracting high resolution LArTPC reconstruction, it does come  
924 with a high computational cost. This was an issue for generating a large sample of Monte

Table 7.1: CORSIKA MC rates

Neutron induced 1 $\pi^0$	1,255
Neutron induced 1 $\pi^0$ outside	13,434
Proton induced 1 $\pi^0$	5,038
Other induced 1 $\pi^0$	9,530
no 1 $\pi^0$ or multi $\pi^0$	61,040

925 Carlo for Wire-Cell imaging. The process should be able to be distributed, but for this anal-  
 926 ysis it this process was not yet available. This required us to use an up-sampling technique  
 927 with the background Monte Carlo sample which is describe in the subsequent paragraphs.

928 First a enhanced sample of 1,255 signal events were generated from CORSIKA, processed  
 929 through wire-cell imaging, and reconstructed with the described process in section 6. A  
 930 background only sample, consisting of 8,720 randomly sampled background events were  
 931 processed through wire-cell imaging and the reconstruction. This number was then scaled by  
 932 0.0139 to obtain an absolute background value relative to the enhanced signal sample. This  
 933 scaling represents a new total of 90,297 events. One event corresponds to one MicroBooNE  
 934 readout frame.

935 From the total sample we find that 1.39% are signal. The remaining background is  
 936 divided into 5 categories: (1) neutron induced events that are produced outside the fiducial  
 937 volume, (2) proton induced events that produce 1  $\pi^0$  either inside or outside the fiducial  
 938 volume, (3) Events that produce 1  $\pi^0$  either inside or outside the fiducial volume not coming  
 939 from a proton or neutron, (4) Multi  $\pi^0$  produced either inside or outside the fiducial volume,  
 940 (4) Events that do not contain any  $\pi^0$ . Table 7.1 shows the corresponding counts from the  
 941 90,297 CORSIKA sample.

942 Next, the selection cuts described in chapter 6 are applied to both the signal sample and  
 943 Monte Carlo. There are a total of 443 events that pass the cuts made in section 6. This  
 944 corresponds to a signal efficiency of 35.9%. A plot for the reconstructed mass is shown in  
 945 figure 7.1. The mass peak, which is supposed to be around  $135 \text{ MeV}/c^2$ , is centered around  
 946  $100 \text{ MeV}/c^2$  due to the missing energy. This is in agreement with what we expect from the  
 947 single particle  $\pi^0$  studies from section 6.

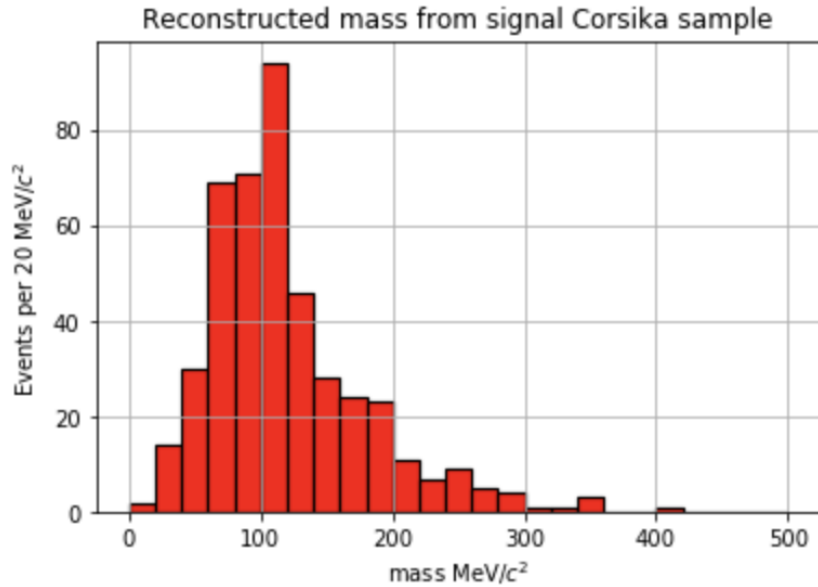


Figure 7.1: Plot of the mass distribution for MC neutron induced signal events.

948 Then, the same cuts were applied to the background only sample. We find there to be  
 949 a background rate of 2.3%. Ultimately resulting in a signal:background of 0.21 (Approximate-  
 950 mately 1 : 5.6). A plot of the reconstructed mass distribution for the entire background is  
 951 shown in figure 7.2

952 It is important to note that the background distribution will also contain  $\pi^0$  events. The  
 953 background distribution as described in section 7.1 is plotted in figure 7.2. The distribution  
 954 should also have some well reconstructed  $\pi^0$ . For this analysis, since we did not require the  
 955 use of a vertex there is a sizable portion of background that are actual reconstructed  $\pi^0$ .  
 956 This comes from two primary effects both of which are products of how the reconstruction  
 957 criteria is defined. The first effect is part of the group coming from events with "No  $\pi^0$ "  
 958 group. Many of the events are actual  $\pi^0$  particles but reconstructed out side of the fiducial  
 959 volume. The second effect is in the remaining  $\pi^0$  groups which obviously contains at least  
 960 one  $\pi^0$ . Being that we remove as many track as possible, Many proton and charged pion  
 961 tracks are removed. The in eyes of the selection process a proton or charged pion induced  
 962  $\pi^0$  event has a near identical topology to the signal.

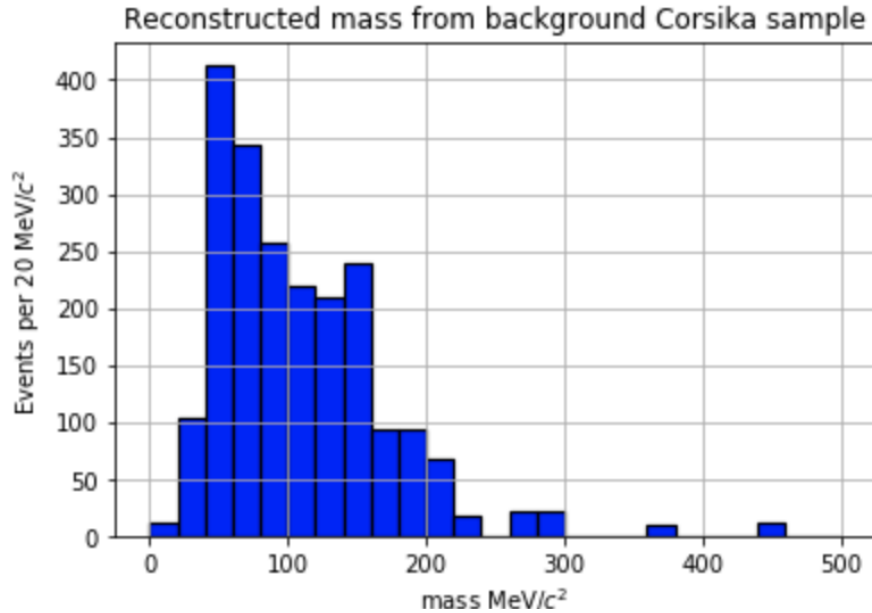


Figure 7.2: Plot of the mass distribution for MC cosmic background events.

## 963 7.2 Data

964 The same selection cuts were applied to a dataset of 13,022 off beam cosmic data events  
 965 that were sampled from the 'MicroBooNE Good Run List'. This is an internal list that  
 966 MicroBoone generates to define when the detector is in acceptable running mode. This list  
 967 takes into account various aspects of the detector such as wire stability, argon purity, PMT  
 968 response, etc. It is important to note that the data sample that is used in this thesis is only  
 969 from the good run list. Doing this, assumes that any bias in the sample is averaged over  
 970 for interaction type. The mass distribution is calculated from the given 13,022 sample and  
 971 there is a clear mass peak from the  $\pi^0$ s that is also centered below the actual  $135 \text{ MeV}/c^2$   
 972 mass.

## 973 7.3 Data-Monte Carlo Comparison

974 To better understand the data distribution, we first plot an area normalized histogram for  
 975 Monte Carlo and Data. This is shown in figure 7.3. We see that the shape is indeed similar  
 976 but not ideal. Given this, the area normalized shape comparison only serves the purpose of

977 showing that we believe we are reconstructing  $\pi^0$ 's and reasonably handling the background.

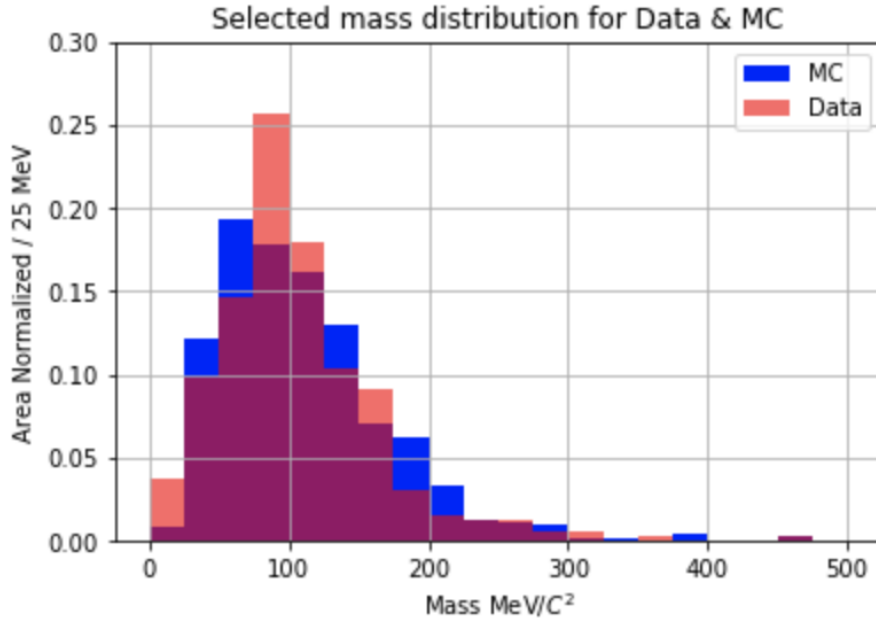


Figure 7.3: Area normalized Data-Monte Carlo mass distributions. The shapes between the data and Monte Carlo distributions provide confidence that we are reconstructing  $\pi^0$ 's in the distribution.

978 To better compare data and Monte Carlo an absolute rate comparison should be made.  
 979 This will address how well the Monte Carlo represents the data. The mass distribution is  
 980 shown in Figure 7.4. Out of the box, CORSIKA slightly over predicts the rate from data  
 981 producing  $\chi^2/df$  of 1.37. To address this, a  $\chi^2$  minimization can be performed fit the Monte  
 982 Carlo to the data. Both the signal and background are varied to optimize the fit to data.  
 983 We will assume a flat 5% systematic error and account for the statistical error of both the  
 984 Monte Carlo and data. We find that the fit returns a minimum of 0.73  $\chi^2/df$  when the  
 985 signal is reduced by 72% and the background is also reduced by 84%. The adjusted mass  
 986 distribution from the fit is shown in Figure 7.5

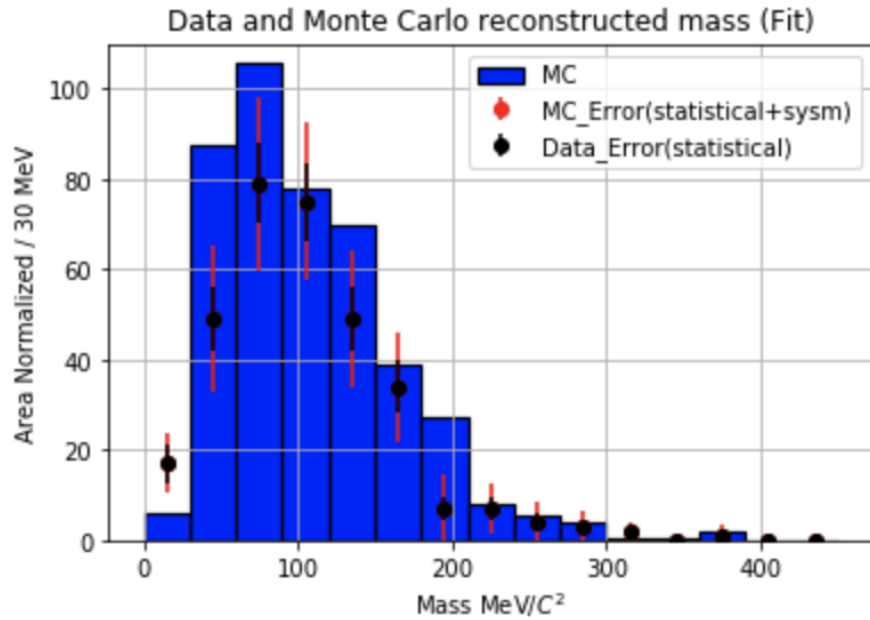


Figure 7.4: This plot shows the mass distribution from data with respect to the unchanged Monte Carlo.

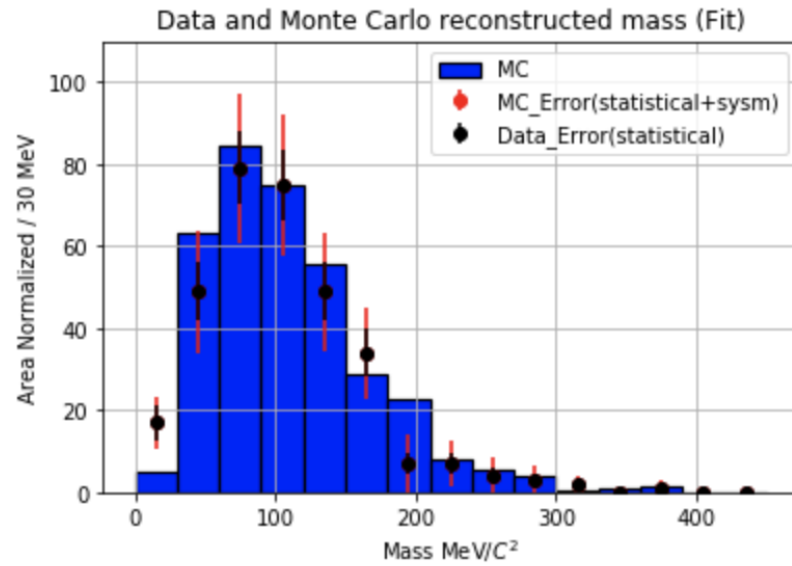


Figure 7.5: This plot shows the mass distribution from data with respect to the fitted Monte Carlo.

# 987 Chapter 8

## 988 Conclusions

### 989 8.1 Conclusion

990 The construction of MicroBooNE is an essential step forward for the low energy neutrino  
991 physics community. The R&D process provided valuable insights towards future LArTPC  
992 detector technology. The MicroBooNE detector was completed in 2015 and has since been  
993 collecting valuable data.

994 This thesis showcases a radically new technique for 3D reconstruction of EM showers.  
995 Although wire-cell does require a high amount of computational resources, the improved  
996 3D reconstruction capabilities for EM showers provide justification. Additionally, we are  
997 able to reconstruct  $\pi^0$ s without the use of vertex information. We have built an algorithm  
998 to identify neutron induced single  $\pi^0$  events. We found that the current CORSIKA Monte  
999 Carlo slightly over predicts the rate of neutron induced  $\pi^0$  in the MicroBooNE detector.  
1000 The data used in this thesis is entirely on cosmic ray data but the extension to a neutral  
1001 current single  $\pi^0$  interaction is the next logical step.

## Part I

## Appendices

SP0TER is located on Github:

<sup>1004</sup>  
[https://github.com/1grossora>Show\\_Sp0ter](https://github.com/1grossora>Show_Sp0ter)

To obtain a copy of the code you first must have git installed. Next clone the repository to a location of your choice by using the command below.

```
git clone git@github.com:1grossora>Show_Sp0ter.git
```

The requirements are located on the readme page above. Base Requirements:

- Root version: 6.05 or greater
- scipy, numpy, sklearn
- Cython

MC or data from MicroBooNE (not public). A list of important parameters are listed below. The values of these parameters were used for this thesis study but can be varied as the users discretion. More documentation can be found on the github repository page listed above.

Parameter Name	Parameter Value	Location	Parameter Description
charge_thres	500	Utils	Threshold value corresponding to wirecell space point charge
nq_thresh	600	Utils	Max number of charge points in a wirecell blob
zlo	400	Utils	Lower bound z distance
zhi	800	Utils	Upper bound z distance
ylo	116	Utils	Lower bound y distance
yhi	-116	Utils	Upper bound y distance
xlo	-1000	Utils	Lower bound x distance
xhi	1000	Utils	Upper bound x distance
make_json	False	Utils	Produce a json for the BEE display
mincluster	20	Reco	Minimum amount of space points

			needed	65
nn_dist 1005	2	Reco	Minimum distance required for a space point to be merged	
birch_leaf	1000	Reco	Max size of a cluster from birch clustering	
birch_min_cluster	20	Reco	Minimum size of a cluster from birch clustering	
edge_dist	1	Merge	Distance require to merge together hulls from birch clusters	
stitch_mincluster	100	Merge	Minimum number of space points requires to be considered a cluster after stitching	
vari_0	0.9985	Track	Value of the first charge weighted pca of the cluster	
ts_fcl_length	20	Track	Minimum length of hull to designate as a shower	
ts_fcl_minsize	10	Track	Minimum size of the hull to designate as a shower.	
Doca_sweep	10	Shower	Minimum length between two end points of two clusters	
lcmin	25	Shower	Minimum length showers for a final merged shower	
vari_1	0.998	Shower	Value of the second charged weighted PCA of the cluster	
ts_scl_length	25	Shower	Minimum length of shower	
ts_scl_minsize	10	Shower	Minimum volume of the size of showers	
snn_dist	2	Shower	Final showers within this distance are merged.	

# Bibliography

- 1006
- 1007 [1] Henri becquerel biography. 2014.
  - 1008 [2] W. Pauli. Open letter to the group of radioactive people at the gauverein meeting in  
1009 tubingen. 1930.
  - 1010 [3] S. Schael et al. Precision electroweak measurements on the  $Z$  resonance. *Phys. Rept.*,  
1011 427:257–454, 2006.
  - 1012 [4] C. Patrignani et al. Review of Particle Physics. *Chin. Phys.*, C40(10):100001, 2016.
  - 1013 [5] D. DeCamp and B. Deschizeaux et al. Determination of the number of light neutrino  
1014 species. *Physics Letters B*, 231(4):519 – 529, 1989.
  - 1015 [6] C. Rubbia. The Liquid Argon Time Projection Chamber: A New Concept for Neutrino  
1016 Detectors. 1977.
  - 1017 [7] S. Amerio and S. Amoruso. et al. Design, construction and tests of the icarus t600 de-  
1018 tector. *Nuclear Instruments and Methods in Physics Research Section A: Accelerators,*  
1019 *Spectrometers, Detectors and Associated Equipment*, 527(3):329 – 410, 2004.
  - 1020 [8] C. Anderson et al. The ArgoNeuT Detector in the NuMI Low-Energy beam line at  
1021 Fermilab. *JINST*, 7:P10019, 2012.
  - 1022 [9] H. Chen et al. A Proposal for a New Experiment Using the Booster and NuMI Neutrino  
1023 Beamlines: MicroBooNE.

- 1024 [10] Pip Hamilton. First Measurement of Neutrino Interactions in MicroBooNE. In *18th*  
1025 *International Workshop on Neutrino Factories and Future Neutrino Facilities Search*  
1026 (*NuFact16*) *Quy Nhon, Vietnam, August 21-27, 2016*, 2016.
- 1027 [11] The microboone technical design report. 2012.
- 1028 [12] R. Acciarri et al. Design and Construction of the MicroBooNE Detector. *JINST*,  
1029 12(02):P02017, 2017.
- 1030 [13] Teppei Katori. The MicroBooNE light collection system. *JINST*, 8:C10011, 2013.
- 1031 [14] Costas Andreopoulos, Christopher Barry, Steve Dytman, Hugh Gallagher, Tomasz  
1032 Golan, Robert Hatcher, Gabriel Perdue, and Julia Yarba. The GENIE Neutrino Monte  
1033 Carlo Generator: Physics and User Manual. 2015.
- 1034 [15] A. A. Aguilar-Arevalo et al. The Neutrino Flux prediction at MiniBooNE. *Phys. Rev.*,  
1035 D79:072002, 2009.
- 1036 [16] A. Aguilar-Arevalo et al. Evidence for neutrino oscillations from the observation of anti-  
1037 neutrino(electron) appearance in a anti-neutrino(muon) beam. *Phys. Rev.*, D64:112007,  
1038 2001.
- 1039 [17] A. A. Aguilar-Arevalo et al. The MiniBooNE Detector. *Nucl. Instrum. Meth.*, A599:28–  
1040 46, 2009.
- 1041 [18] A. A. Aguilar-Arevalo et al. Unexplained Excess of Electron-Like Events From a 1-GeV  
1042 Neutrino Beam. *Phys. Rev. Lett.*, 102:101802, 2009.
- 1043 [19] J. S. Marshall and M. A. Thomson. The Pandora Software Development Kit for Pattern  
1044 Recognition. *Eur. Phys. J.*, C75(9):439, 2015.
- 1045 [20] R. Acciarri et al. Convolutional Neural Networks Applied to Neutrino Events in a  
1046 Liquid Argon Time Projection Chamber. *JINST*, 12(03):P03011, 2017.
- 1047 [21] Xin Qian, Chao Zhang, Brett Viren, and Milind Diwan. Three-dimensional Imaging  
1048 for Large LArTPCs. *JINST*, 13(05):P05032, 2018.

- 1049 [22] D. Heck, G. Schatz, T. Thouw, J. Knapp, and J. N. Capdevielle. CORSIKA: A Monte  
1050 Carlo code to simulate extensive air showers. 1998.
- 1051 [23] S. Agostinelli et al. GEANT4: A Simulation toolkit. *Nucl. Instrum. Meth.*, A506:250–  
1052 303, 2003.